

Synergy and fusion of optical and synthetic aperture radar satellite data for underwater topography estimation in coastal areas

Andrey Pleskachevsky · Susanne Lehner ·
Thomas Heege · Claudius Mott

Received: 15 December 2010 / Accepted: 15 June 2011 / Published online: 19 July 2011
© Springer-Verlag 2011

Abstract A method to obtain underwater topography for coastal areas using state-of-the-art remote sensing data and techniques worldwide is presented. The data from the new Synthetic Aperture Radar (SAR) satellite TerraSAR-X with high resolution up to 1 m are used to render the ocean waves. As bathymetry is reflected by long swell wave refraction governed by underwater structures in shallow areas, it can be derived using the dispersion relation from observed swell properties. To complete the bathymetric maps, optical satellite data of the QuickBird satellite are fused to map extreme shallow waters, e.g., in near-coast areas. The algorithms for bathymetry estimation from optical and SAR data are combined and integrated in order to cover different depth domains. Both techniques make use of different physical phenomena and mathematical treatment. The optical methods based on sunlight reflection analysis provide depths in shallow water up to 20 m in preferably calm weather conditions. The depth estimation from SAR is based on the observation of long waves and covers the areas between about 70- and 10-m water depths depending on

sea state and acquisition quality. The depths in the range of 20 m up to 10 m represent the domain where the synergy of data from both sources arises. Thus, the results derived from SAR and optical sensors complement each other. In this study, a bathymetry map near Rottneest Island, Australia, is derived. QuickBird satellite optical data and radar data from TerraSAR-X have been used. The depths estimated are aligned on two different grids. The first one is a uniform rectangular mesh with a horizontal resolution of 150 m, which corresponds to an average swell wavelength observed in the 10×10-km SAR image acquired. The second mesh has a resolution of 150 m for depths up to 20 m (deeper domain covered by SAR-based technique) and 2.4 m resolution for the shallow domain imaged by an optical sensor. This new technique provides a platform for mapping of coastal bathymetry over a broad area on a scale that is relevant to marine planners, managers, and offshore industry.

Keywords SAR · TerraSAR-X · QuickBird optical images · Underwater topography

Responsible Editor: Michel Rixen

This article is part of the Topical Collection on *Maritime Rapid Environmental Assessment*

A. Pleskachevsky (✉) · S. Lehner
German Aerospace Center, Remote Sensing Technology Institute,
Oberpfaffenhofenhofen-Wessling,
Münchener str. 20,
82234 Wessling, Germany
e-mail: Andrey.Pleskachevsky@dlr.de

T. Heege · C. Mott
EOMAP GmbH & Co. KG, Sonderflughafen Oberpfaffenhofen,
Friedrichshafener Str. 1,
82205 Gilching, Germany

1 Introduction

In this paper, the different remote sensing data are combined to collect the underwater topography in coastal areas worldwide. In spite of the fact that the worldwide bathymetry should already be known, and there are no “blank spots” on global maps, at least for one-nautical-mile-resolution data sets (e.g. global topography by NOAA (a 30-arc-s (1 km) gridded, quality-controlled global Digital Elevation Model (DEM) <http://ngdc.noaa.gov/mgg/topo/globe.html>), ETOPO 1-Minute Global Relief, NOAA) the local depth variation, e.g., sand bank, bars, and reefs on the

one hand and the temporal morphodynamical development of seabed structures on the other hand, can be significant in littoral zones. E.g., in the German Bight (North Sea), the soft seabed topography can change relatively fast due to storms (Flampouris, 2010) so that the official charts can be quite out of date.

Generally, the remote sensing techniques to obtain high-resolution bathymetry can be divided into two groups based on the physical background of algorithms:

- (1) Depth estimation from remote sensing data based on sunlight reflection analysis and governed by chemical and physical characteristics of sea water, e.g., the bottom reflection. This kind of investigation is covered by optical methods: processing optical satellite data allows the physical approximation of water depths by correcting sun glint, atmospheric effects, and the influence of the water column on the earth observation data (Heege et al., 2008).
- (2) Depth estimation based on observation of hydrodynamic processes, which are influenced by topography in a different way and thus reflect the underwater structures. This group of technique can be performed using SAR (e.g., Bruschi et al. 2010, Li et al., 2006, Fan et al., 2008), RAR (marine Real Aperture Radar, e.g., WAMOS, Hessner et al., 1999), and optical data (Piotrowski and Dugan, 2002).

In the paper, both of the techniques mentioned are applied. The investigations are carried out near Rottenest Island, Australia, where SAR and optical and echo sounding in situ measurement data are available. The area investigated is indicated by a sliced shoreline and a complicated underwater topography which includes numerous underwater reefs and is a real challenge for an algorithm of “robustness test”.

The paper is structured as follows: in the “Introduction” the bathymetry estimating techniques are briefly discussed and the area investigated is described. “Section 2” deals with SAR methods and results by TS-X. In “Section 3” the optical methods are implemented for shallow water depth estimation. “Section 4” presents the fusion of bathymetry derived from SAR and optical data. The discussion in “Section 5” treats the question of applicability for the SAR-based and optical methods.

1.1 Depth from optical data

The first technique is applied by depth estimation from optical remote sensing data, e.g., by QuickBird or RapidEye satellites images. According to numerous studies, the assessment of water depth using optical remote sensing data is a reliable and cost-efficient method in shallow water (Green et al. 2000, Lafon et

al. 2002, Vanderstraete et al. 2003, Heege et al. 2007). A significant challenge connected to remote sensing of shallow water areas is that the water column overlying the substrate significantly affects the remotely sensed signal due to optical attenuation of light in water (Mobley 1994). Remotely sensed water color cannot be interpreted directly as variation in water depth, water quality, or habitat because the signal is not exclusively associated with any of these parameters (Holden and LeDrew 2002). Any serious attempt of interpreting remotely sensed data relies on mathematical or radiative transfer modeling (Philpot 1987). Thus, remote sensing from aircraft or satellites has a great potential for assessing water constituents and bathymetry but always requires correction for atmospheric, air–water interface, and water column effects. The details are presented in “Section 3”.

1.2 SAR data and depth estimation by circulation currents

The techniques based on the observation of hydrodynamic processes use the effect of modification of surface currents and ocean waves by bathymetry. Since both of them are influenced by underwater topography in coastal areas, the change of their properties reflects the underlying depths. As the physical background is known and the connection between observed characteristics and topography can be applied, the depth maps can be derived.

The local circulation currents are governed by the law of conservation of mass in the first place; their acceleration in the shallows is connected to underwater structures. The changing of currents, in turn, produces a change of surface roughness and this effect can be imaged by remote sensing. Since the launch of the SEASAT satellite in 1978, a series of investigations of ocean features by space-borne SARs have been performed and a method based on change of water surface reflection by strong surface currents was presented by Alpers and Hennings (1983) and Hennings (1990). As mentioned, this SAR-based method to estimate underwater topography uses the effect of variation of circulation currents: if a strong current flows over a sand bank, the speed of the current is higher over the ridge than before or after due to the law of conservation of mass. Due to this interaction, the spatially changed currents affect the roughness of the surface by small-scale Bragg waves which are responsible for the radar backscatter of the sea surface. Thus, underwater bottom topography becomes visible in SAR images by modulating the image brightness (Romeiser and Alpers 1997). Using this approach, one can only compute the relative spatial changes of the underwater bottom topography. To obtain the complete bathymetry map, the input of water depths are required for several reference points from external data sources.

1.3 SAR data and depth estimation by refraction of long swell waves

In this paper, a new approach to retrieve bathymetry from SAR images is used. The long ocean waves propagating towards the coastal line are investigated. Since the launch of the new German satellite TerraSAR-X in 2007, radar data of a new quality stage with high spatial resolution up to 1 m allow the use of new techniques. Ocean surface waves can be resolved down to a wavelength of about 30 m (Bruck and Lehner, 2010). High-resolution TS-X images allow the measurement of individual long-wave properties, refraction, shoaling effects, etc. due to improved SAR parameters. SAR image analysis via Fast Fourier Transformation (FFT) results in directional image spectra. From these spectra, the peak wavelength and the directions of swell waves visible in the image are extracted (Brusch et al., 2010).

The wave propagation presents the conversation of the energy flux, influenced still by energy dissipation due to bottom friction and breaking (relates to the peak period as well). The wave energy flux is the power transported by wave action and given by

$$F_w = E_w C_g \quad (1)$$

where E_w is the mean wave energy density per unit horizontal area. E_w is the sum of potential and kinetic energy density, proportional to wave amplitude a squared and $E_w = 0.5 \cdot g \rho a^2$ for a monochromatic wave (g is gravitational acceleration and ρ means water density). C_g is the wave group velocity (function of wave period). Thus, in shallow areas, depth-forced wavelength shortening is compensated by a wave amplitude increase. This phenomenon is commonly known as shoaling effect. An increase of wave height can be roughly estimated using shoaling coefficient and occurs until the wave steepness exceeds a certain threshold where wave breaking takes place.

Since the wavelength can be mathematically connected with local depth via the dispersion relation equation, depth can be estimated from swell wavelength observations. In the case of static SAR data, wave frequency must be obtained from external sources or by calculating it with a first-guess for the water depth. Details and usage information are presented in “Section 2”.

1.4 Depth estimation by using the synergy of SAR and optical data

Both techniques: depth estimation from optical information for extra-shallow water and non-direct technique using SAR data have been effectively tested in different areas (Brusch et al. 2010), however a combination of their

results into an aggregate product is the new topic presented in this paper.

Depth data sets obtained from optical images (QuickBird) and from SAR (TerraSAR-X) are combined in order to cover different depth domains. The SAR-based and optical approaches to estimate bathymetry make use of different physical backgrounds and have different mathematical implementations and acquisition conditions. The SAR-based methodology uses long wave refraction; it cannot be applied during calm weather conditions during which optical methods are preferred. The waves produce seabed erosion and influence light attenuation in the water column by suspended matter. Otherwise, the results from SAR and optical data complement each other: The optical methods provide reliable depths in domains up to 20 m (the results are depending on the specific inherent optical properties of the analyzed water body). The depths estimation from SAR cover domains of about 70–10 m, obtained from wave behavior, and is dependent on wave properties and acquisition quality (Brusch et al. 2010). The depth between 10 and 25 m is the potential synergy domain; data from both sources can be compared and integrated. The details and results are presented in “Section 4”.

1.5 Study area Rottenest Island, West Australia

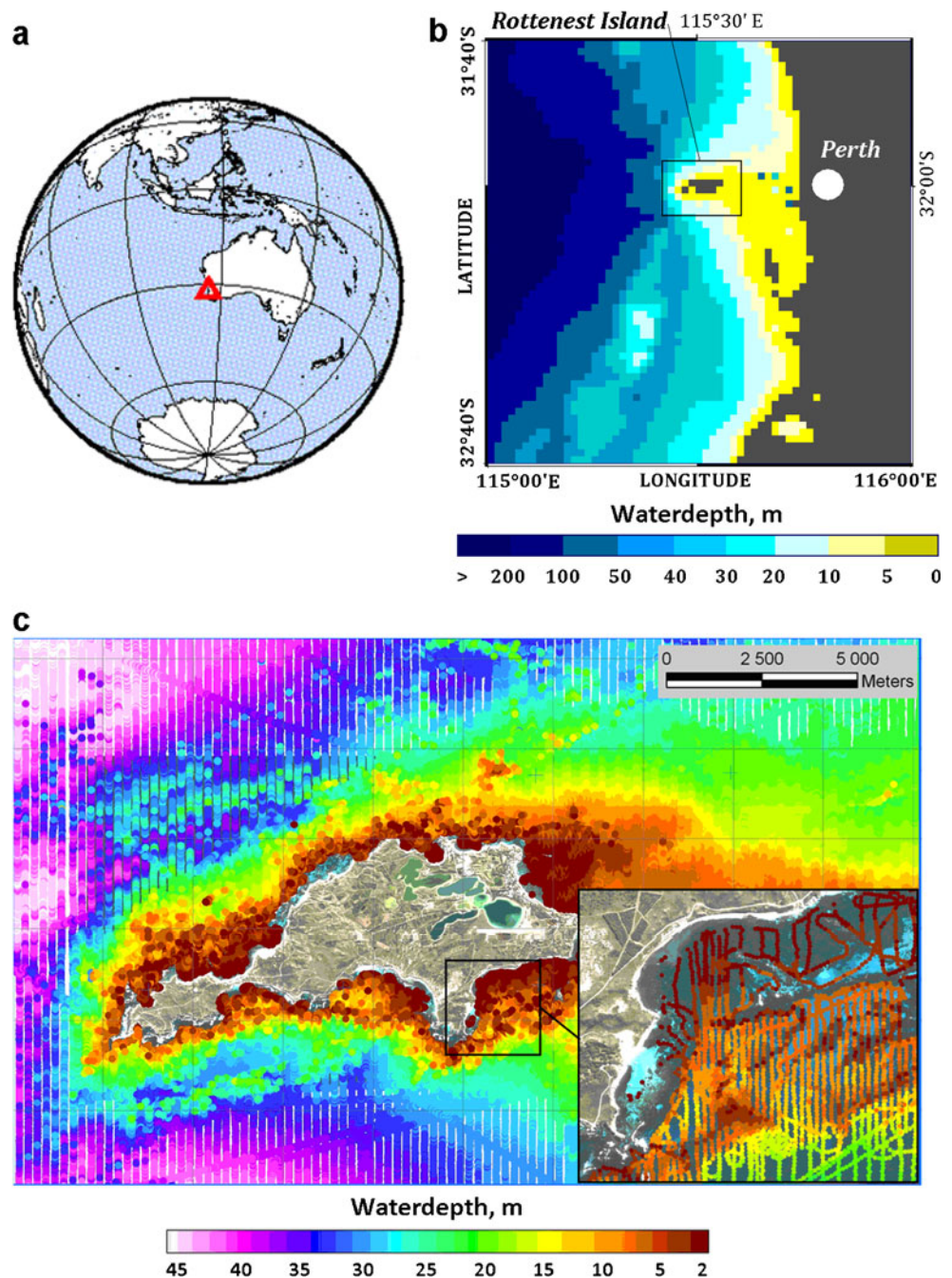
In this paper, the underwater topography for the Rottenest Island, Australia, is investigated. The selection of this domain has several backgrounds:

- (1) Depth data from sonar measurements of fine spatial resolution are available.
- (2) The water attenuation (the island is a fossilized coral reef) allows for depth estimation using optical data in the coastal zone.
- (3) The storms in the south-west of Australia create a well-developed and reliably forecasted long swell directed to the study area.

Rottenest Island is situated about 50 km off the coast of Western Australia (Fig. 1a; 115°30' E, 32°00' S) near the city of Perth. The island is about 10.5 km in length and 4.5 km in width and located on the relatively flat continental shelf off the Perth coastline. The island presents the seaward end of the shallow Murray Reef System; thus, the western end of Rottenest Island can be considered as a headland. The notch of the angular-shaped shelf edge, which is the beginning of the Perth submarine canyon, is located off the island's western end (Alaee et al., 2007).

Figure 1b shows the coarse depth field (ETOPO 1-Minute Global Relief; NOAA, NGDC's *GEO*physical *DATA* System, <http://www.ngdc.noaa.gov/mgg/gdas>). Figure 1c presents the measurements from a ship-installed echo depth

Fig. 1 Rottenest Island, Australia, located on the globe (a), ETOPO 1-Minute Global Relief by NOAA (b), and in situ ship echo sounding measurements by Murdoch University, Perth (c)



sonder with a high spatial resolution of about 10 m, provided by the Western Australian Department for Planning and Infrastructure and processed by Murdoch University, Perth, WA, Australia. The island is composed of quaternary limestone and dune sand. Fringed by limestone reefs, the island's topography is temporally quite stable (Playford and Leech, 1976). The coastal line is sliced and the depths fall strongly around the island up to about 50 m in the space of about 1 km. A coral reef belt around the island appears in the form of underwater benches and bars. Nutrient and chlorophyll concentrations in the sea

water around the island are low in comparison with those of other typical west coast situations (Pearce et al., 2006).

As the Rottenest Island is arranged in front of the Southern Australian coast margin, it is exposed to the largest waves of the global ocean, having been generated by Southern Ocean extra-tropical storms (Hemer et al., 2007). Rottenest exhibits mostly southerly wave directions, reflecting the greater distance from the Southern Ocean generating storms, and demonstrates highly energetic extreme events, a predominance of swell over wind sea states. The island represents interest in terms of ecology and

oil industry: Perth already has three large oil exploration leases near Rottenest Island.

2 Underwater topography estimation by TerraSAR-X

This section aims to obtain underwater topography using SAR information from TerraSAR-X images. The general questions of SAR imaging of sea surface and SAR-based techniques to retrieve the swell properties are discussed (details are presented in “Appendix”). The bathymetry is estimated from SAR information using the effect of a long wave’s refraction, a comparison with in situ echo sounding measurement data, and errors are given.

2.1 SAR imaging of sea surface created by waves

Synthetic aperture radar SAR is an active remote sensor which provides two-dimensional information of the normalized radar cross-section σ_0 (NRCS). The principle of synthetic aperture is to replace a snapshot of a large antenna with many images of a small, moving antenna installed on, e.g., a satellite. Making use of the rapid platform motion, airborne or space-borne SAR systems achieve a high resolution both in flight (azimuth) and across flight (range) direction. If the path of the real antenna is known and the scenery is static, one can synthesize a large antenna aperture from the intensity and phase of the received radar echoes and a high spatial resolution in the azimuth direction can be achieved (for more details, see “Appendix”).

The NRCS represents the ability of a surface to reflect the radar signal and is defined as the normalized energy flux scattered by a unit area of the surface into a given direction. The backscatter is governed by the surface roughness on the scale of the radar wavelength, which is $\lambda_{\text{SAR}}=3.1$ cm for the TS-X SAR, and the dielectric properties of the imaged object. With incidence angles between 20° and 55° , the SAR signal falls into the Bragg regime following Bragg condition:

$$\lambda_B = 0.5\lambda_{\text{SAR}} \sin \theta \quad (2)$$

where θ is the SAR signal incidence angle. If the roughness of the surface imaged approximately satisfies the Bragg condition, constructive interference in the direction of the sensor occurs.

In the case of surface waves, the radar return echo is dominated by Bragg scattering of short ripple capillary waves, in the order of centimeters, produced by wind at sea surface (e.g., Schulz-Stellenfleth et al., 2001). Conventionally, the SAR imaging mechanism of sea surface created by waves as described in literature (e.g., Hasselmann et al. 1985) bases on real aperture radar (RAR) mechanism with

additional specifics connected to SAR and consists of three main parts:

- (1) The local radar backscattering mechanism, which is governed by the sea surface roughness on a centimeter scale (short waves created by wind called Bragg waves). In case of total lack of wind (total calm weather condition), the surface is smooth and reflects the radar signal aside, but not to the sensor; from a mirror surface, the sensor get no radar echo and swell waves cannot be imaged.
- (2) The modulation of the local backscatter processes by long waves (longer than twice the SAR resolution cell) as described by the RAR.
- (3) The impact of Doppler shift of surface facets imaged (velocity bunching effect), which is associated with wave motion towards the SAR sensor.

The dominant RAR modulation mechanisms are presented by, e.g., Schmidt (1995) and Alpers and Rufenach (1979):

- (1) Tilt modulation: long waves modulate the surface slope. The local incidence angle θ of the radar signal is changed and the radar return is influenced according to the Bragg condition (Eq. 2).
- (2) Hydrodynamic modulation: This interaction (due to the wave orbital motion of longer waves) leads to the modulation of energy contained in the Bragg waves: wave crest and trough are moving in opposite directions; the zones of convergence and divergence of local velocities occur, leading to the shortening and stretching of capillary surface waves. This results in changes of the sea surface roughness.
- (3) Range bunching: a geometric effect which leads to the modulation of SAR image intensities associated with surface slopes caused by waves. This effect is more important for a radar system installed not high over the water surface. Moreover, e.g., for ship-installed radar, one wave can screen the wave behind.

In summary, SARs image ocean waves, especially long swell waves, by measuring the sea surface roughness and slope, which influence radar echo. Due to their high resolution, daylight and weather independency, and global coverage, space-borne SARs of new generation are particularly suitable for many ocean and coastal applications (Lehner et al., 2008). In the presented paper, the data from TS-X are used (Breit et al., 2010) (for more details about SAR imaging of ocean waves by TS-X and the statistics, see “Appendix”).

2.2 TerraSAR-X satellite and acquiring of swell waves

The German X-band SAR satellite TS-X was launched in June 2007 (www.dlr.de/TerraSAR-X). Since January 2008,

data and products are available for researchers and commercial customers. TS-X operates from a 514-km-height sun-synchronous orbit. The TS-X ground speed is 7 km s^{-1} (15 orbits/day). It operates with a wavelength of 31 mm and a frequency of 9.6 GHz. The repeat cycle is 11 days, but the same region can be imaged with different incidence angles after 3 days depending on the latitude. There are four different imaging modes with different spatial resolutions; the technical parameters of the different modes are provided in Table 1. The resolution of the TS-X images has been visibly improved in comparison to earlier SAR missions (about 2 m for Spotlight mode against 25 m for ENVISAT ASAR). The typical incidence angles for TS-X range between 20° and 60° .

Compared to earlier SAR missions like ENVISAT ASAR, TS-X offers, besides a higher resolution, a number of further advantages: e.g., the Doppler shift of a scatterer, moving with velocity u_r toward the sensor (radial velocity) at distance R_0 (slant range), is reduced. For instance, for the same incidence angle 22° and $u_r=1 \text{ ms}^{-1}$, the target's displacement in azimuth direction $D_x = (u_r/V_{\text{sar}}) \cdot R_0$ is reduced by a factor of about 2 and results in $\sim 73 \text{ m}$ for TS-X ($\sim 115 \text{ m}$ for ENVISAT) due to a different platform velocity V_{sar} (7.55 km s^{-1} for ENVISAT) and a slant range R_0 (ENVISAT altitude is 800 km) (Lyzenga et al., 1985). Figure 2 shows examples for TS-X with different modes acquired over Rottenest Island: VV polarized Stripmap on September 23, 2009 at 10:53 UTC and Spotlight on October 20, 2009 at 21:36 UTC.

The analysis of TS-X images can be used for the following oceanographic applications: ship-, ice-, oil-, and underwater shallow area (bank and bars) detection, obtaining wind, coastal line, and underwater topography fields (Lehner et al., 1998). In the following, we use the TS-X Spotlight images with coverage of 10 km by 10 km. For this mode, the SAR azimuth resolution is improved by pointing the antenna towards the specific target area (spot) during overflight. This increases the time–bandwidth product and improves the resolution. Figure 3 shows the effect of the achieved higher resolution comparing images of ENVISAT with a pixel size of 12 m to TS-X images. The ENVISAT scene was acquired on December 21, 2008 over Rottenest Island; the sub-scenes for the location in front of the east coast of the Island are shown for TS-X Spotlight, Stripmap, and ENVISAT. Although the waves are detectable in ASAR images, the extraction of wavelength $<200 \text{ m}$ and

obtaining refraction of quality necessary for underwater topography estimation are not possible (for the zoomed image, see “Appendix”; Fig. 15).

The Spotlight TS-X SAR image acquired over Rottenest Island on October 20, 2009 is shown in Fig. 4. The long swell waves induced in the ocean due to a storm (storm peak of about 1,500 km south-west from the area 3 days before) and propagating towards the island are visible in the TS-X image and the refraction is well pronounced. The scene was specially ordered to acquire the long swell waves for bathymetry estimation. The wave forecast model WAVEWATCH-III (NOAA, http://polar.ncewaves/waves/viewer.shtml?multi_1-latest-hs-aus_ind_phi-) was used to determine the appropriate acquisition time. The forecasting information was applied 1 week before TS-X image acquisition.

The ocean waves represent a periodic displacement of the sea surface. The linear wave theory describes the sea state as a superposition of elementary *cos*-waves $j=1, N$, which are propagating in $0\text{--}360^\circ$ directions. The surface elevation by one wave component is:

$$\zeta_j = a_j \cdot \cos(k_j x - \omega_j t + \varphi_{0j}) \quad (3)$$

where $a_j=0.5H_j$ is the j -wave amplitude with wave height H_j , $\omega_i=2\pi f_j=2\pi/T_j$ (T_j is the wave period) is the angular frequency for frequency f_j , $k_i=2\pi/L_j$ the wave number, φ_{0j} is the initial phase, L_j is the wavelength, x means the horizontal coordinate, and t is the time. The whole 2D surface elevation can be presented as a function of location $\vec{r}(x,y)$ and time:

$$\zeta(\vec{r}, t) = 0.5 \cdot \sum_{j=1}^N \left[a(\vec{k}, \omega) e^{i(\vec{r}\vec{k}_j - \omega_j t)} + a^*(-\vec{k}, -\omega) e^{-i(\vec{r}\vec{k}_j - \omega_j t)} \right], \quad (4)$$

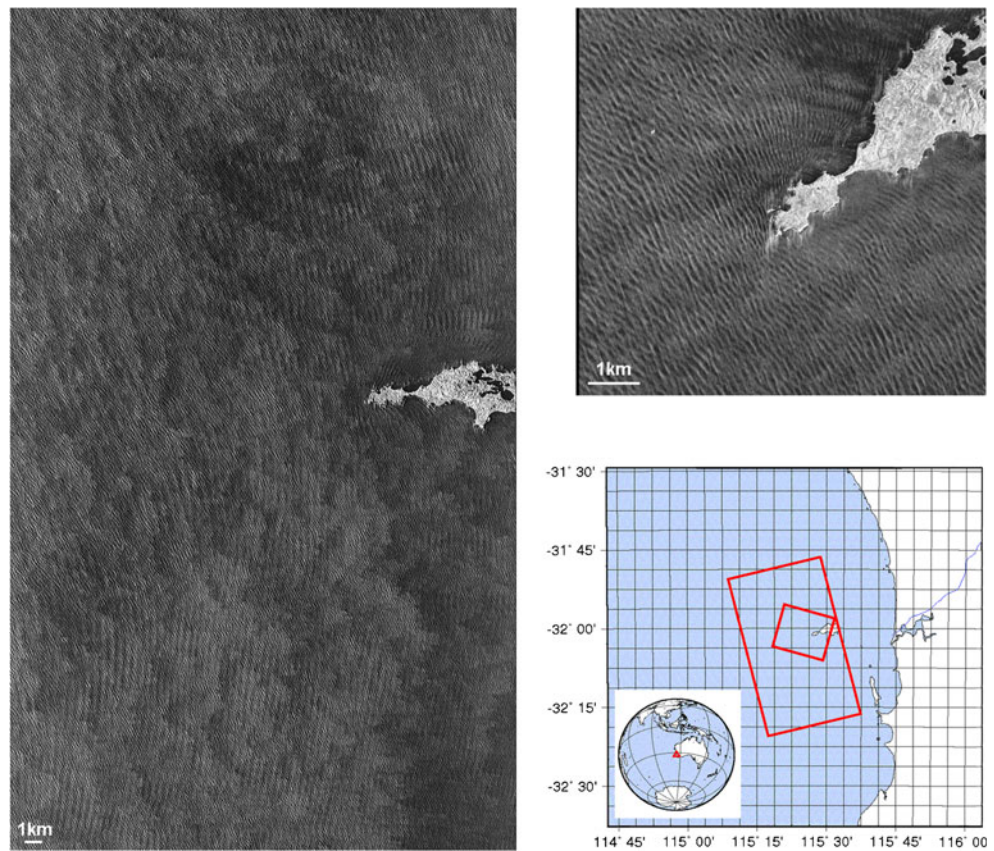
where Fourier coefficients a and a^* are complex and complex conjugated amplitudes, including phase information and wave number vector $\vec{k}_j = (k_x, k_y)$. The wave action is mathematically described using a wave spectrum which presents a distribution of wave energy (proportional to wave height squared) in the direction and frequency (or wave number) domain. Proper integration of spectra results in integral wave parameters as significant wave height, mean period, and direction.

The sub-images in Fig. 4 show the NRCS and random surface simulation for a location. The surface is obtained by

Table 1 TerraSAR-X imaging modes

	ScanSAR	StripMap	Spotlight	High-resolution spotlight
Swath width (ground range)	100 km	30 km	$10 \times 10 \text{ km}$	$5 \times 10 \text{ km}$
Azimuth resolution	18 m	3.3 m	2 m	1.7 m
Range resolution	1.7–3.5 m	1.7–3.5 m	1.5–3.5 m	1.5–3.5 m

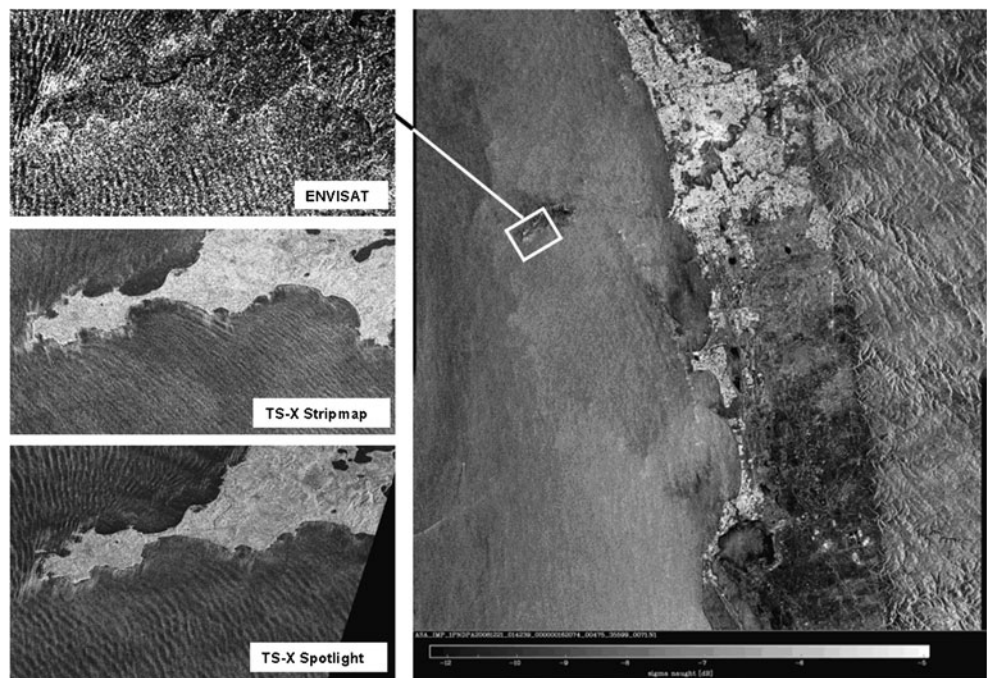
Fig. 2 Different modes of TS-X images acquired over Rottenest Island: VV polarized Stripmap on September 23, 2009 at 10:53 UTC (*left*) and Spotlight on October 20, 2009 at 21:36 UTC (*right*)



applying the linear wave theory (Eq. 4) to a wave spectra simulated using a spectral numerical wave model (Schneggenburger et al., 2000). To study the wave refraction and surface elevation, the numerical simulations are carried out on a grid with a horizontal resolution of 150 m (bathymetry

is based on NOAA interpolated dataset; Fig. 1b). The spectral numerical model inputs are the local wind field and boundary spectra (swell part from SAR information, wind sea using JONSWAP spectra as a function of obtained wind and fetch) estimated from TS-X Rottenest Island scene

Fig. 3 Effect of achieved resolution by TerraSAR-X. ENVISAT ASAR image from December 21, 2008 acquired over Rottenest Island (*right*). TS-X Stripmap and Spotlight images sub-scenes from Fig. 2 (*left*)



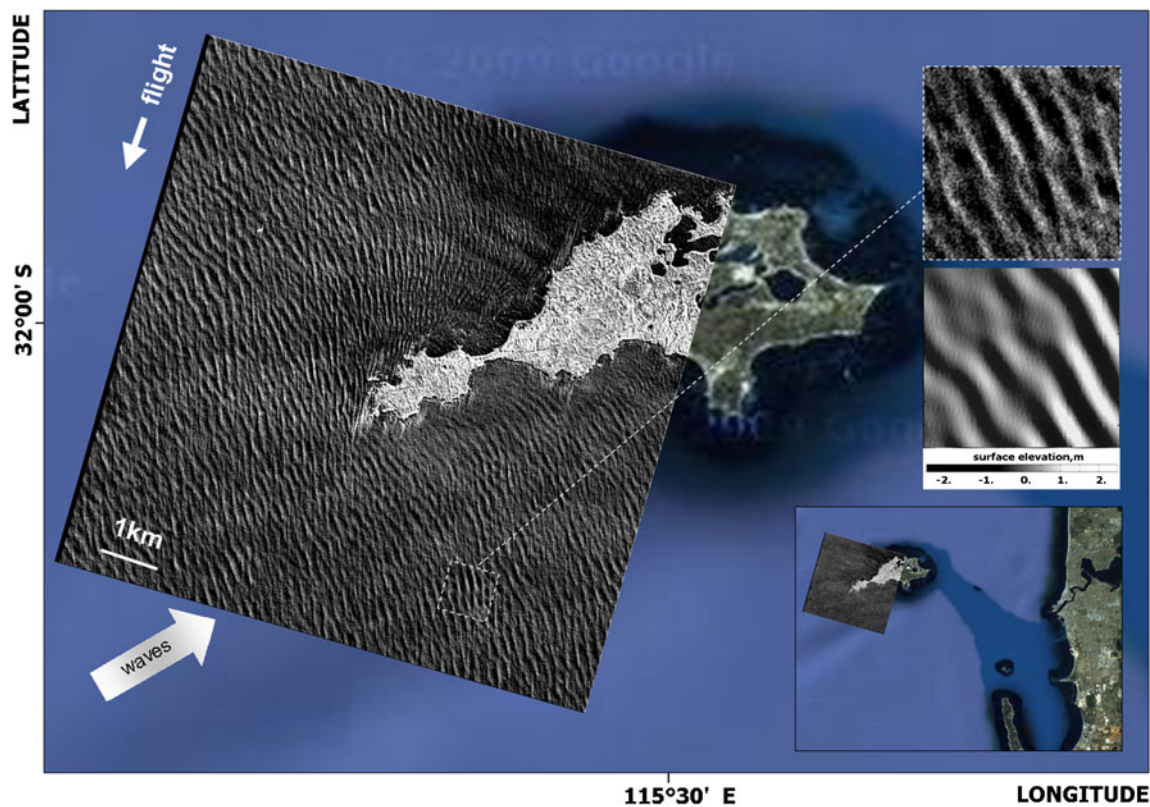


Fig. 4 TerraSAR-X Spotlight at 10 km by 10 km coverage acquired on October 20, 2009 over Rottenest Island Australia (background image © Google Map). A sub-scene (*top right*) shows the details of

the wave structures and random surface elevation obtained from wave spectra simulated by a numerical model

(XMOD and XWAVE algorithms; Lehner et al., manuscript submitted for publication). It is important to note that, although the wave imaging mechanism for TS-X is non-linear, the replacement of the facets by Doppler shift remains inside one wavelength by the swell wave for TS-X characteristics and acquisition properties (ground speed, slant range, and wave traveling direction) according to the theory. Although a single wave is imaged “turned” in its own location, its image is focused around a wave crest. Thus, the imaged waves keep the original wavelength values (for more details, see “Appendix”).

2.3 Refraction of long wave and its tracking to obtain underwater topography

The method is based on an observation of consecutive waves along their propagation from a start point up to the coast. The wave-rays technique is already well known and widely used as an application for the wave model results (e. g., Winkel, 1994). The wave rays can be obtained also from wavelength and wave direction observed on SAR images.

Figure 5 shows a scheme of the method: around a selected point on the image (start point of the wave track), a sub-image is selected. By computing the FFT analysis for the selected sub-image, a two-dimensional image spectrum in

wave number space is retrieved. The peak in the 2D spectrum marks a mean wavelength and a mean wave direction of all waves was visible in the sub-image. Values for wavelength and angle of wave propagation can be estimated as follows:

$$L_P = \frac{2\pi}{\sqrt{k_{P_x}^2 + k_{P_y}^2}}, \quad \theta_P = \arctan\left(\frac{k_{P_y}}{k_{P_x}}\right) \quad (5)$$

where L_P is the peak wavelength, θ_P is the peak wave direction with respect to the image (azimuth direction) and k_{P_x} and k_{P_y} are the image spectra peak coordinates in wave number domain with axes x =satellite flight direction (azimuth) and y =range. The retrieved wave directions have an ambiguity of 180° due to the static nature of a SAR image. This ambiguity can be resolved using SAR cross-spectrum or first-guess information from other sources. In coastal areas where wave shoaling and refraction appear, the propagating direction towards the coast is visible on the image.

Starting in the open sea, the box for the FFT is moved in the wave direction by one wavelength (or with a constant specified shift) and a new FFT is computed. The procedure is repeated until the corner points of the FFT box reach the shoreline. This way, waves can be tracked from the open sea to the shoreline and changes of wavelength and direction can be measured (Fig. 5a).

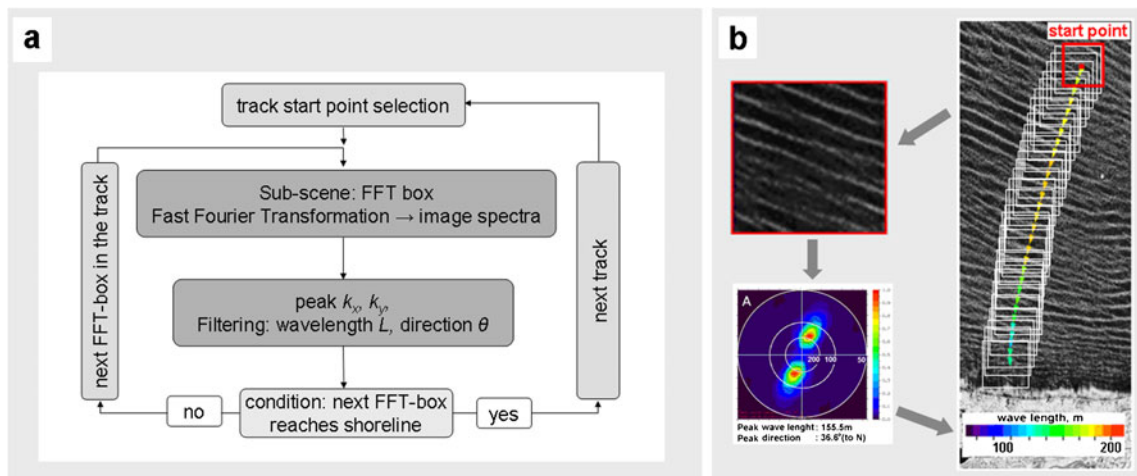


Fig. 5 Algorithm for tracking wave rays: by computing the Fast Fourier Transformation for a sub-image, a 2D image spectrum is retrieved in wave number space. The peak in the 2D spectrum marks the wavelength and wave direction. Starting in open sea, the box for the FFT is moved in the wave direction and a new FFT is computed.

Data filtering is taken into account for the wave direction (cross sea) and wavelength (wind sea and wind streaks). The procedure is repeated until the corner points of FFT-Box reaches shoreline (a); an example of one wave ray (b)

Figure 5b shows a principle of tracing and an example of one tracked wave ray. Wind streaks (structures on the sea surface of the image produced by airflow turbulent eddies at the boundary layer) and wind sea patterns are removed from the spectra by filtering the wavelengths between about 80 and 300 m (background values must be checked for every scene). After moving the FFT box to the next point in the swell propagation direction, the next peak is restricted to not deviate by more than $\pm 15^\circ$ compared to the previous peak direction in order to avoid switching to another wave system in case of cross-sea.

To retrieve water depth, the linear dispersion relation for ocean gravity waves was applied. The solution of the dispersion relation with respect to water depth d :

$$d(L_P, \omega_P) = \frac{L_P}{2\pi} \operatorname{atanh} \left(\frac{\omega_P^2 L_P}{2\pi g} \right) \quad (6)$$

where ω_P is the angular wave peak frequency ($\omega_P = 2\pi/T_P$, T_P is the peak period). The method was approved for different areas and sea states (Brusch et al., 2010, Pleskachevsky et al., 2010), i.e., for the Duck Research Pier (North Carolina, USA), Port Phillip (Melbourne, Australia), and around Helgoland Island (German Bight, North Sea).

Where surface currents occur, the dispersion relation, which connects the depth with wave number and frequency, must be modified (Komen et al., 1994):

$$\omega_j^2 = gk_j \tanh(k_j d) + Uk_j \quad (7)$$

where U is a component of the surface currents to j -wave propagation direction. In this study, the effect of current can

be neglected since the currents are weak (in the order $0.01\text{--}0.05 \text{ ms}^{-1}$ in the area around Rottenest Island; Alaei et al., 2007). The shallow areas where the long shore current effects appear (e.g., due to wave breaking-induced flow) are taken out from processing. These areas are covered by depth estimation using optic-based methods.

Figure 6a shows examples of obtaining one wave ray for the Rottenest Island Spotlight scene. A total of 40 wave rays overlapping the area are shown in Fig. 6b. The numerical simulation using the spectral wave model is carried out on a grid with a horizontal resolution of 150 m (see “Section 2.2”). The model results (Fig. 6c) present significant wave height and direction. The refraction and shoaling near the coast (strong increase of wave height) are indicated. Generally, the refraction at the coast by model agrees well with observations, except for local effects: e.g., an area located in the north. Since the reef bank (see echo sounding observation; Fig. 1c) in the north of the Island is not present in the coarse NOAA bathymetry, no refraction occurs at this location in model simulation.

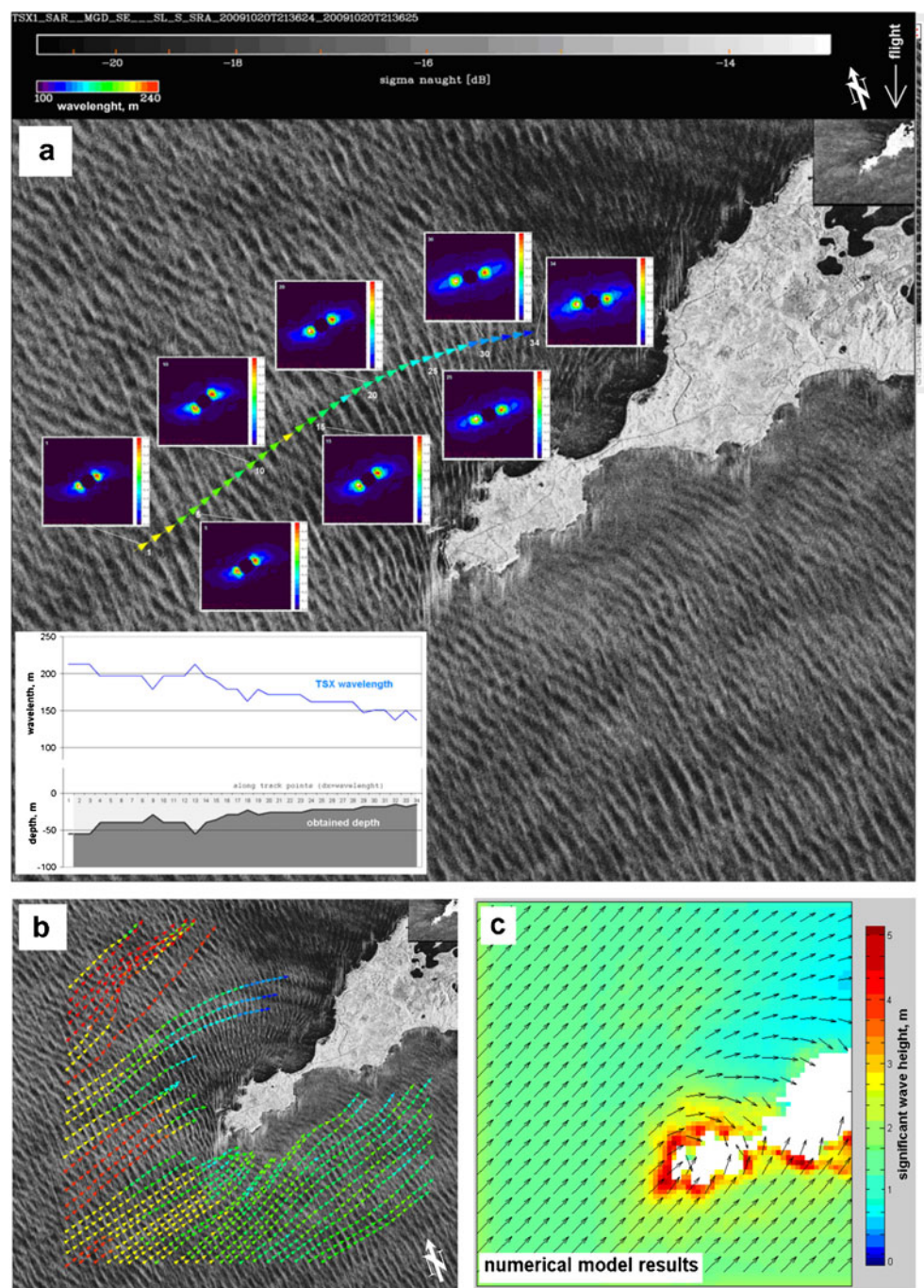
2.4 Estimation of underwater topography using TerraSAR-X data

For practical use, obtaining topography is divided into five workflow steps:

- (1) Scene first-check: simulation of some wave tracks (e.g., ten reference tracks). Reference tracks overlap the study domain in different areas. First-checking

Fig. 6 TerraSAR-X Spotlight acquired over Rottenest Island (Fig. 5). NRCS and one wave track with exemplifying image spectra are shown (a).

Sub-scene shows the wavelength along the track and obtained underwater topography for its trajectory. In the *top right* corner, the quick look of the scene is shown. There were 40 wave rays overlapping the area as shown (b). A numerical simulation (c) presents significant wave height and refraction (direction shown by *arrows*); model inputs are wind field and the boundary was estimated from TS-X data; horizontal resolution is 150 m; bathymetry is based on NOAA dataset, Fig. 1b). The shoaling areas are presented by a strong increase of wave height; since the bank in the north of the Island is not present in the course of NOAA bathymetry, no refraction occurs at this location in the model simulation



is applied to evaluate the validity of the scene and to obtain the threshold for filtering of wavelengths and directions. Further, the peak period is estimated: this determination is based on a combination of first-guess for the depths and analysis of reference-tracks.

- (2) Obtaining wavelength map using wave ray technique: a dense coverage of the area with wave tracks. For a uniform mesh (150-m resolution), 400

wave rays were necessary for sufficient dense area coverage.

- (3) Obtaining wavelength using raster method: in the areas where coverage of wave tracks is not dense enough, a raster approach is used: the FFT boxes are moved not in the wave direction but at a certain distance dx and dy .
- (4) Obtaining resulting wavelength field: after filtering, wavelength is interpolated, extrapolated, and

smoothed on a uniform grid (a reasonable resolution for topography is the averaged wavelength; for Rottenest Island, the raster $dx=dy=150$ m was applied).

- (5) Estimation of corresponding depths: using the dispersion relation, the depth field is derived.

The peak period needed in Eq. 6 is obtained using a combination of first-guess and analysis of the tracks ($T_p=13.25$ s). The longest observed wave in the image is $L_{\max}=245$ m. The threshold for minimal peak period for this wavelength, obtained from deep water relation $T_p^{\min}=(2\pi L_{\max}/g)^{0.5}=12.25$ s (solutions of dispersion relation in Fig. 14 show that, for periods smaller than 12.5 s, a wave of length 245 m belongs to the deep water domain, where it cannot be influenced by the bottom conditions. Then, again, the wavelength changes in the SAR image that evidences the bottom influence; thus, $T_p > T_p^{\min}$).

Figure 7 shows the scene processing results: derived wave field (Fig. 7a), derived underwater depth field (rectangular mesh of 150 m horizontal resolution, shown in 3D; Fig. 7b). Figure 7c presents the scheme for the comparison of retrieved data with sonar measurements: The TS-X scene is underlying; a white line marks the area for which a comparison is done. The sonar measurement data from different echo sounding campaigns (measurement errors unknown) are also integrated and interpolated on a rectangular uniform grid $dx=dy=150$ m; the relative error between both data sets is shown in Fig. 7d: assuming that the interpolated sonar depths present the real values, then about 50% of the compared area has an error range of about $\pm 10\%$ (shown in white color). There are also more variations (one is located in the north of the island): the swell waves are slowed down and dissipated over a reef and do not build up anymore in a “bag” between two reef banks. The wave breaking zones, in front of the coast, destroy the processing of sub-images and do not allow the wavelength to be obtained accurately. They are masked and taken out from depth estimation processing.

3 Optical data

For processing of optical multispectral satellite data, the Modular Inversion and Processing System (MIP) was used (Heege et al. 2003, Heege and Fischer 2004). MIP is designed for a physical-based assessment of hydro-biological parameters from multi- and hyperspectral remote sensing data. It is used for the environmental mapping of aquatic shallow and deep waters of inland waters, coastal zones, and wetlands. The architecture of

the program binds a set of general and transferable computational schemes in a chain, connecting bio-physical parameters with the measured sensor radiances. The processing system has been applied in many surveys over German inland waters and Australian, Indonesian, and Asian coastal zones, which were performed by airborne and satellite sensors.

3.1 Methods for processing optical data

The different program modules of MIP support the transferable algorithms. The adjustment of algorithms to sensor specifications and recording conditions is supported automatically in MIP (Heege and Fischer 2004). MIP consists of different processing modules, containing adjacency, sun glitter, atmospheric, and water column correction algorithms. A schematic overview on the workflow applied here is displayed in Fig. 8. The algorithms retrieve the underlying variable optical properties in atmosphere and water, including water depth. The modules access to different data bases containing optical models and specific optical coefficients of the atmosphere, the water body, and the sea floor to sensor specific parameters and to a radiative transfer data base.

The radiative transfer data base contains the physical knowledge and relations between important measures, for example, between radiance measured at the sensor (L) and subsurface reflectance R . The relations are stored as a function of wavelength, atmospheric conditions, geometric recording conditions, and optical properties of the water body.

The atmospheric model of MIP is aimed at the regularization of the radiative transfer (RTE) inversion. Atmosphere is therefore characterized by a comparatively low number of parameters and follows the main features of that adopted in MODTRAN code (MODerate spectral resolution atmospheric TRANSmittance algorithm and computer model; Abreu and Anderson, 1996). The model of water composition serves the same aim as the model of the atmosphere. Scattering, backscattering, and absorption coefficients of water bulk are expressed as a linear combination of corresponding location-dependent normalized optical properties of water species with concentrations as the weighting factors. The radiative transfer calculations have to be obtained with high accuracy as only a small part of the total reflected radiance is reflected by water bulk and represents in reality the useful signal. The RTE solver used to build the radiative transfer data base is based on a finite element method. It incorporates a multilayer atmosphere–ocean system (Kisselev and Bulgarelli, 2004).

Atmospheric correction and the transformation of the sensor radiances L to the subsurface irradiance reflectance

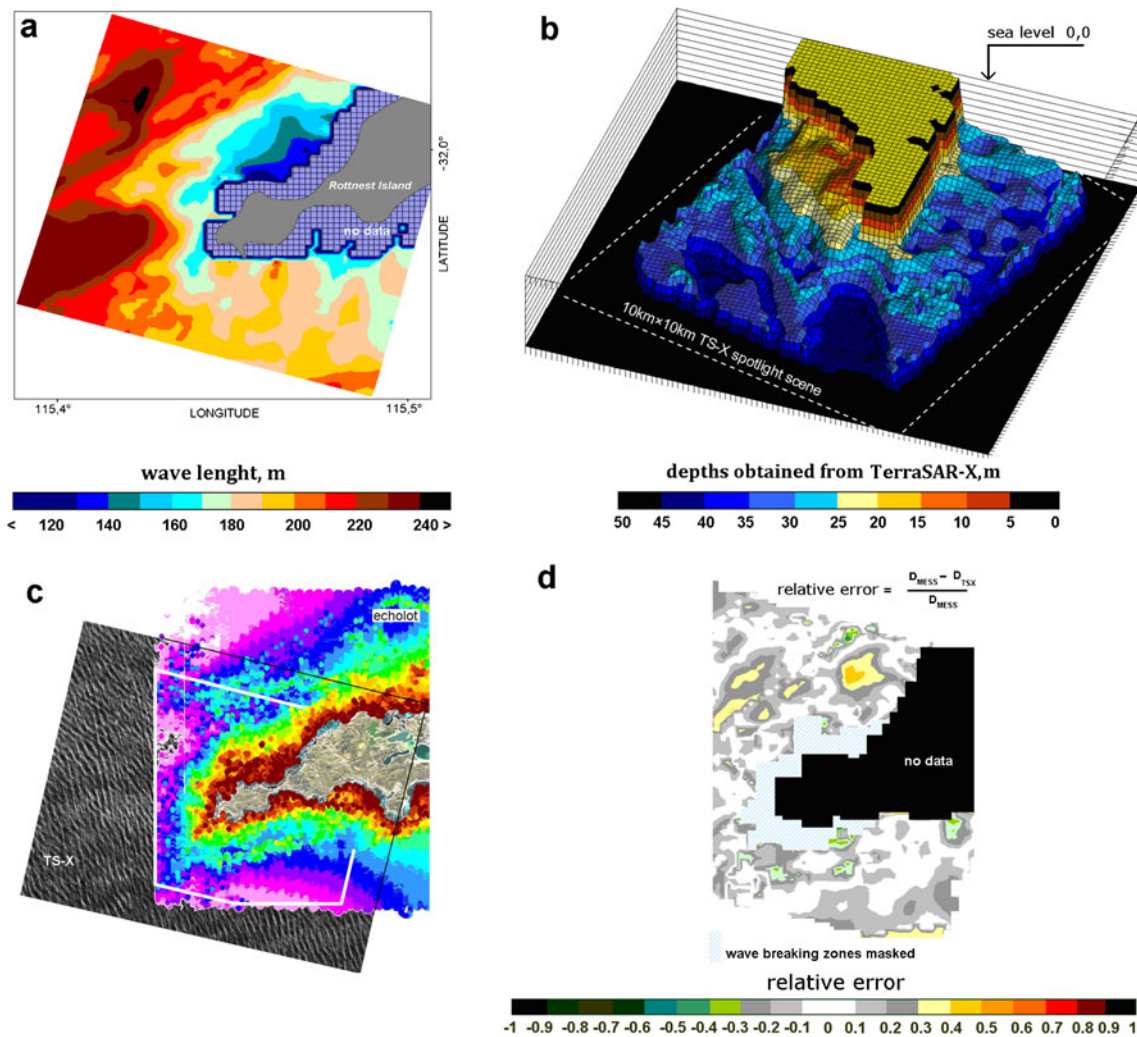


Fig. 7 Wavelength field (uniform raster 150-m resolution) obtained from TS-X scene (a), 3D depth field derived (b), schema for comparison of a sonar measurement to TS-X-derived depths (white

line marks the comparison area) (c), and relative error for white-marked area (wave breaking zones are masked additionally) (d)

R are performed during the coupled retrieval of atmospheric properties and water constituent concentrations (Fig. 8). This retrieval is performed by fitting the simulated sensor channel radiances to those observed (Heege et al. 2009). A bi-directional correction for the underwater light field is applied by the use of the so-called Q database (Heege and Fischer 2004).

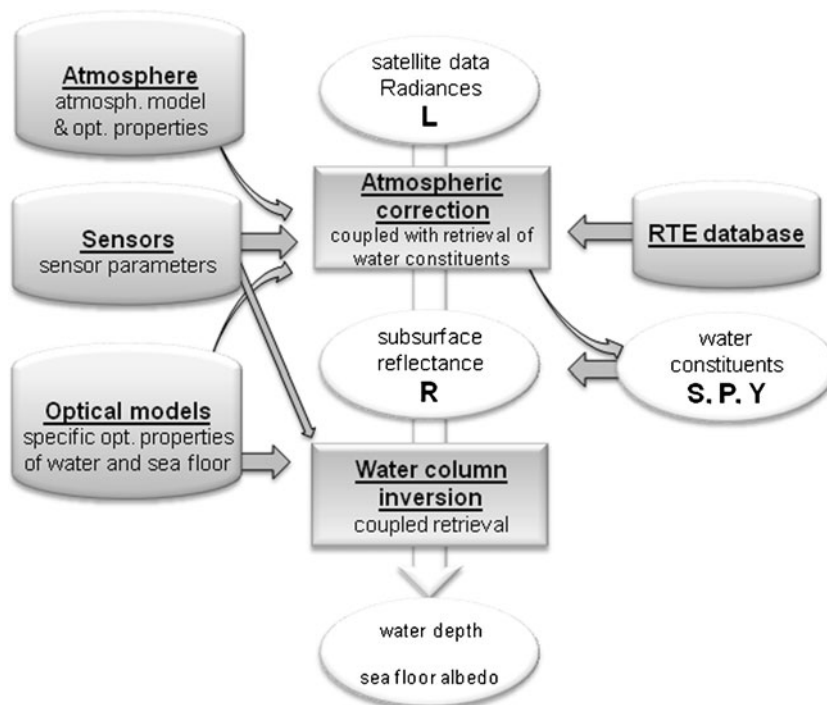
The resulting subsurface reflection R is a function of water depth d , bottom albedo R_b , total absorption a , and scattering b_b of the water and its constituents and of the sun zenith angle θ_s as expressed by the equation published by Albert and Mobley (2003).

$$R = R_\infty \left[1 - A_1 \exp \left\{ - \left(\frac{k_0}{\cos \theta_s} + (1+x)^{k_{1,W}} \left(1 + \frac{k_{2,W}}{\cos \theta_s} \right) \right) (a + b_b) d \right\} + A_2 R_B \exp \left\{ - \left(\frac{k_0}{\cos \theta_s} + (1+x)^{k_{1,B}} \left(1 + \frac{k_{2,B}}{\cos \theta_s} \right) \right) (a + b_b) d \right\} \right] \quad (8)$$

Total absorption a and backscattering b_b in the water column are calculated as products of the specific optical properties and the water constituent concentrations (S, P, Y) that are retrieved in the deep water areas as a first approximation. R_B is the sea floor albedo and A_1 and A_2 are fixed constant values. The attenuation coefficients $x, k_{1,W}, k_{2,W}, k_{1,B}, k_{2,B}$, and the subsurface reflection for the optical deep water case (R_∞) are again functions of a and b_b .

The still unknown value of the water depth d is calculated iteratively in combination with the spectral unmixing of the main spectral classes to the respective calculated bottom reflectance R_B . The unmixing procedure produces the seafloor coverage of three selected main bottom components and the residual error between the model bottom reflectance and the calculated reflectance. The final depth, bottom reflectance, and bottom coverage are achieved at the minimum value of the residual error. Having “input” spectra

Fig. 8 Schematic overview of the workflow for the assessment of bathymetry from multispectral EO data



into the algorithm of the “to be expected” or “actually present” seafloor cover components will improve the end results as demonstrated by Pinnel (2007).

3.2 QuickBird satellite

QuickBird is a high-resolution commercial earth observation satellite owned by DigitalGlobe and launched in 2001. The satellite collects panchromatic (black and white) imagery at 60–70-cm resolution and multispectral imagery at 2.4- and 2.8-m resolutions. It operates at approx. 450 km in altitude and a 98° sun-synchronous orbit. QuickBird records four multi-spectral channels: blue (450–520 nm), green (520–600 nm), red (630–690 nm), and near-IR (760–900 nm).

3.3 Assessing bathymetry with optical data

We analyzed a QuickBird scene recorded on July 17, 2005 and which was provided by Murdoch University, Perth, Australia. Murdoch University provided as well an extensive set of reference data for Rottnest Island. More than 50,000 echo sounding measurements in near-coast areas were provided and used for the accuracy assessment. The workflow presented in Fig. 8 was applied without the incorporation of additional ground truth measurements. Additional ground truth measurements are usually not needed due to the completely physically based structure of MIP if the sensor calibration is accurate. However, the final quantitative values of the data product bathymetry are still adjusted by empirical depth-dependent scaling factors that were estimated consistently

from a number of satellite-based water depth retrievals with the presented method worldwide.

3.4 Bathymetry obtained from optical data

Figures 9 and 10 display the resulting bathymetric chart in comparison to a bathymetric map generated with an echo sounding device. The satellite bathymetry values range from 0.1 to 22 m. Depth differences of 10 cm can clearly be identified in the shallow water regions of the coast. Obvious errors are sparsely distributed and visible in the region of breaking waves and white caps. Hence, doing such a survey in calm-sea-state conditions is desirable.

The comparison with the echo sounding map (where the error bar was unknown) indicated that bathymetry was determined successfully with a relative error of 20% up to a depth of 18 m. Further data products such as the seafloor coverage of the main components give reasonable results but are not to be compared with ground truth. The satellite data clearly provides more detail than the echo sounding map of the same area in shallow water areas below 5 m. Several benthic structures are virtually “blown away” through the interpolation of the sounding data. It seems obvious that the boat carrying the echo sounder could not pass over very shallow reef areas (Fig. 10, circles). At depths more than 10 m, we realize an increase of noise in the satellite-derived map. The retrieval does not deliver stable results at depths more than 18 m in this study. The physical limitation of methods for optical deep waters does not allow much higher values to be retrieved at least for the radiometric sensitivity of IKONOS.

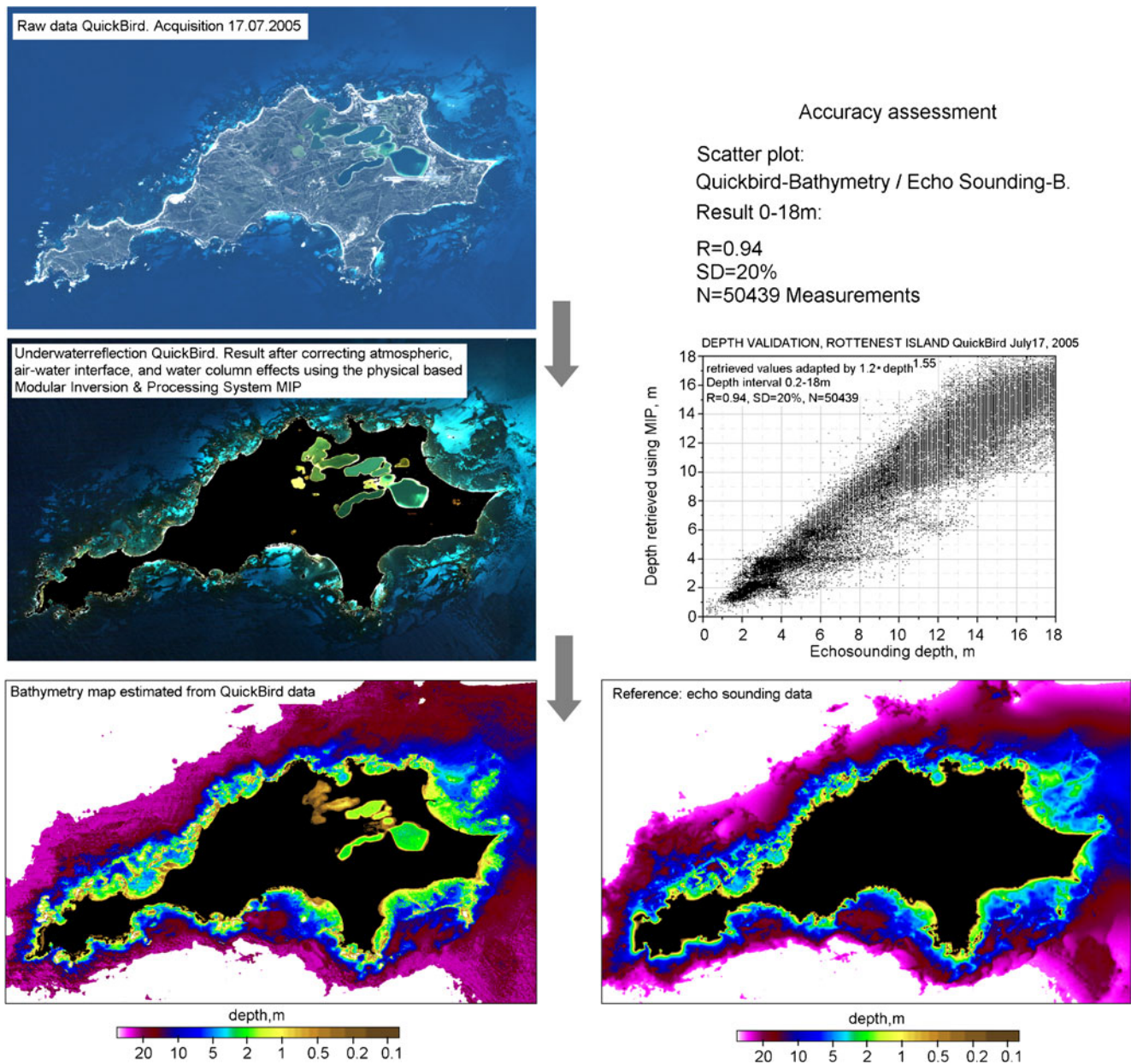


Fig. 9 Workflow bathymetric analysis

4 Fusion and synergy of SAR and optical data

The Synthetic Aperture Radar (SAR) satellite and optical data provide underwater structures and fields in different depth domains. This section aims to integrate the depths derived from SAR and optic.

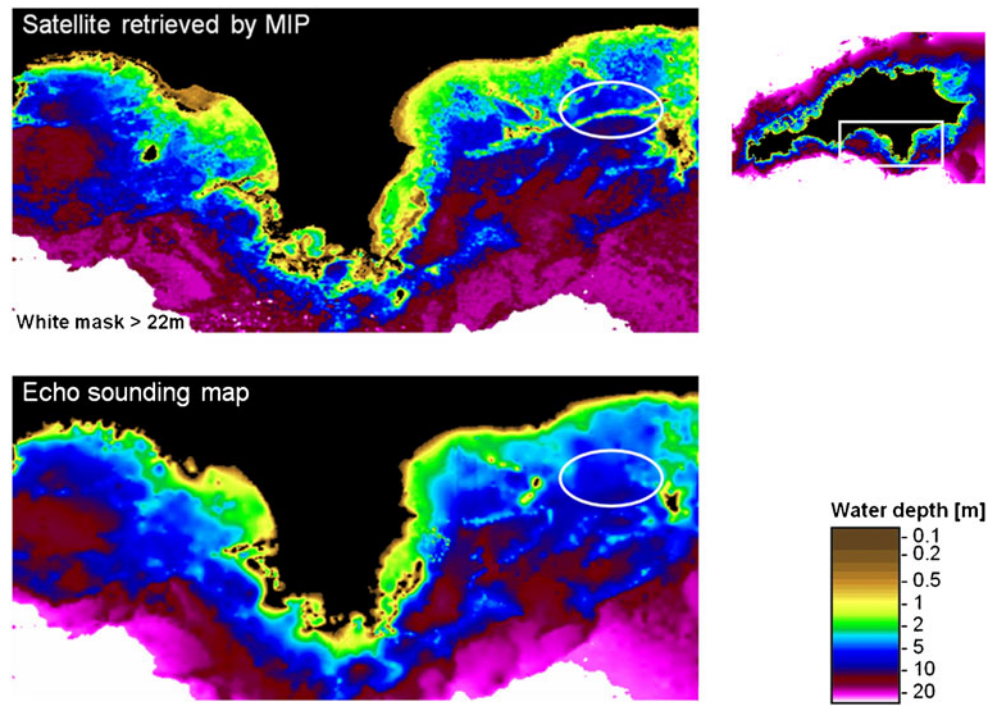
4.1 Synergy and data fusion approach

The depth estimation from SAR covers the areas between about 100- and 10-m water depths, depending on sea state and acquisition quality. The optical methods require other physical

conditions, the SAR-based methods, and provide the depths shallower than 20 m. The depths between 10 and 25 m are a potential synergy domain where data from both sources can be incorporated. In order to obtain incorporated depth field, the study area is divided into three sub-areas:

1. SAR data domain: an area deeper than about 20 m. In this area, only the SAR data can be used; as for optical methods, the seabed is too deep.
2. Synergy area with depths between about 20 and 10 m. In this region, the estimated depths from SAR and optic overlap each over.

Fig. 10 Satellite-retrieved bathymetry (*upper*). Bathymetry based on echo sounding (*lower*). Obvious differences (*encircled*)



- Optical data domain: coastal shallow waters shallower than 10 m; in this area, only optical data can be applied; the swell waves become nonlinear and break.

Figure 11 shows the approach for the study area (150 m raster; the black line on the image marks the area where the depths from SAR are obtained).

The obtained depth information (“Sections 2.2 and 3.2”) can be applied to provide different products: uniform raster, which corresponds to the resolution of SAR-based data (150 m by 150 m, case A). Original resolution from both sources can also be stored; the resulting field keeps original non-uniform information 150 m by 150 m for SAR domain and 2.4 m for optical and synergy domains (case B).

4.2 Bathymetry on a uniform raster

In order to obtain the depth field for a uniform raster (case A), the optical data must be averaged for the coarser resolution and incorporated with SAR-obtained data. Different methods for data combination can be used, e.g., method of optimum interpolation (e.g., Lionello and Günther 1992). This method is widely used for data assimilation. The resulting depth D_A^i for a grid cell i can be obtained as follows:

$$D_A^i = D_S^i + \sigma_S^i \sum_{j=1}^{Nobs} W_{ij} \frac{D_O^j - D_S^j}{\sigma_S^j} \quad (9)$$

where depth D_A^i at each grid point i is produced using a linear combination of D_S^i (SAR-based depth) and D_O^i (depth

from optic). The simplification by definition of coefficients σ_S^i and W_{ij} leads to a reductive formula for a coarser grid (150 m):

$$D_A^i = D_S^i + 0.5 \left(\bar{D}_O^i - D_S^i \right) \quad (10)$$

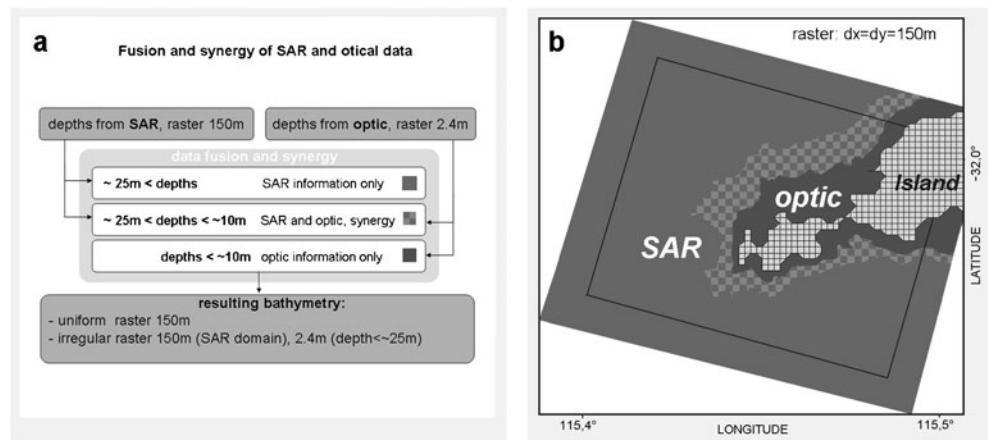
where \bar{D}_O^i is the simple average of optical data for i -cell in 150-m raster used for the synergy of both data sets. More complete investigation of σ_S^i and W_{ij} for TS-X and Quick-Bird data will be done in the future.

Figure 12 presents the resulting depth filed on a uniform rectangular raster of 150-m horizontal resolution. The depth between 60 and 20 m is based on SAR data only; the depths lower than 20 m are a combination of SAR and optical information. The presented underwater depth field includes bathymetry up to the mean sea level and can be combined with above-water topography. Thus, the data from TanDEM-X mission can be incorporated in order to retrieve the complete digital elevation model.

4.3 Bathymetry on a non-uniform raster

The data are combined also without averaging and keeping original information. Figure 13 shows the data aligned on an irregular mesh (150 m for SAR domain and 2.4 m for optic domain). The borderline between the two data sets was defined by visual means at a depth of 18 to 20 m, where the results of the “optical” depth analysis start to decrease in reliability.

Fig. 11 Scheme of data fusion and synergy of optical and SAR data (a). The scene is divided into three domains for data integration (b)



5 Discussion

In this chapter, the applicability of SAR and optical techniques to retrieve underwater topography is discussed.

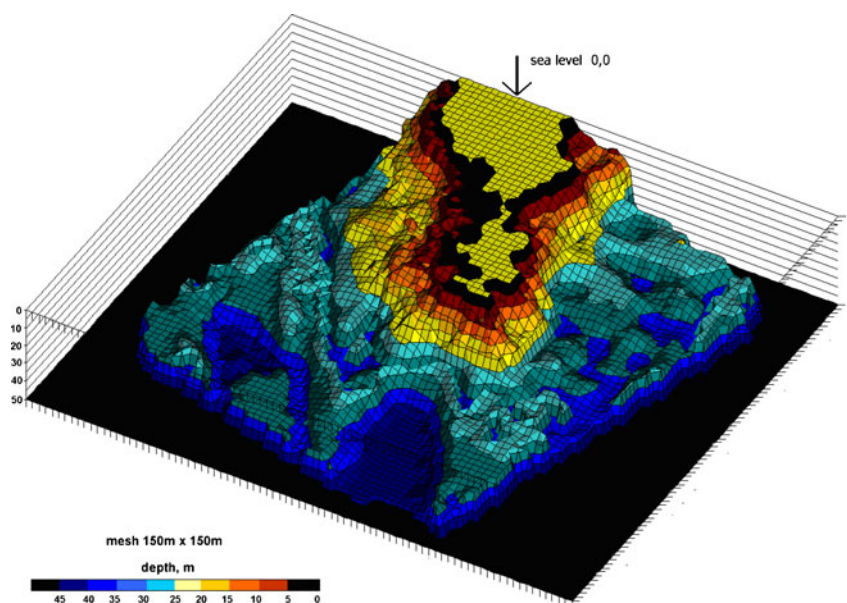
5.1 SAR method based on long wave refraction

The topography estimation for different areas shows that the SAR method is practically applicable if swell waves with height over 0.5 m are present in the wavelength range >80 m (Brusch et al., 2010). As long as the orbital velocity profile of the wave reaches the seabed, wavelength will be modified. This takes place for depths less than 70 m for swell waves of about 200 m in length generally. The solutions of dispersion relation for different wavelength L (50–400 m) and periods (5–20s) are presented in Fig. 14. In TS-X SAR images, the swell wavelength is observed to be in range 80–350 m and representing depth in the range of

about 10–120 m (Brusch et al., 2010). Longer waves with a higher period occur rarely in coastal areas (e.g., in North Sea), however their appearance is quite possible, especially in front of an ocean coast. This allows depth measurements up to about 200 m.

In the North Sea, the duration of swell is relatively short and its prediction is more difficult in comparison to the open coast of Australia where the storms are longer and the coasts are not protected by islands. However, an acquisition of long waves is possible as well: e.g., in a TS-X scene acquired in the North Sea on February 25, 2009 over Helgoland Island, swell waves of about 0.3–1 m in height are depicted as propagating towards the coast of the German Bight. The simulated wave rays show a definite connection with underlying depths and shallows, although the depth estimation cannot be completely processed for the whole scene. The information derived from the scene is insufficient to retrieve the precise depth map but more than

Fig. 12 Depth field obtained from TS-X SAR and optical QuickBird data after fusion and synergy were applied on uniform raster with a horizontal resolution of 150 m by 150 m. The resulting bathymetry field covers the area of about 8 km by 8 km



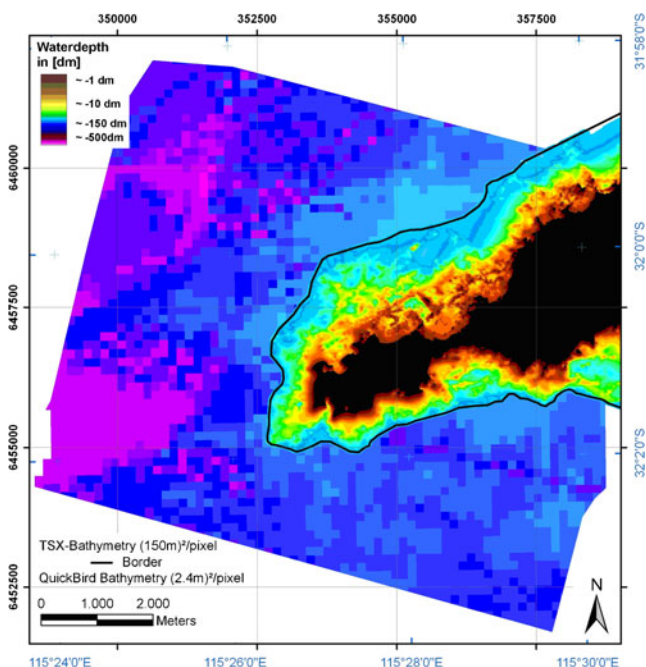


Fig. 13 Depth field obtained from TS-X and optical data applied on non-uniform raster (150 m for SAR domain and 2.4 m for optical domain)

sufficient to detect underwater bars and sandbanks (Lehner et al., manuscript submitted for publication). This kind of information is important for German Bight, where the soft seabed can be changed relatively fast due to storms so that the official charts can be out of date: it is technically complicated and costly to measure in situ the entire German Bight frequently.

The SAR images include non-linear effects by imaging of moving sea surface. The origin of these structures is

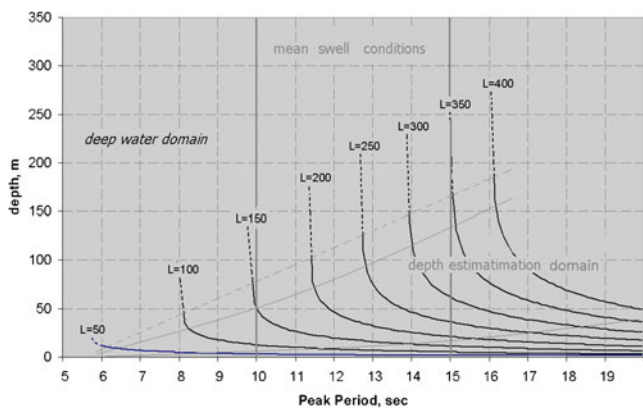


Fig. 14 Dispersion relation for wavelength 50–400 m. The domain where the swell waves react to the depth change and the latter can be estimated is shown. In TS-X SAR images, the swell wavelength is observed to be in the range 80–350 m and representing a depth in range of about 10–120 m (Brusch et al., 2010). Longer waves with a higher period occur rarely, but their appearance is quite possible, especially in front of an ocean coast. This allows depth measurements of up to about 200 m

connected to the displacement of the moving objects by Doppler shift and can be divided in two groups:

1. Reflection of water particle moving inside of the water body with corresponding wave orbital velocity: their projection to satellite (radial velocity) can be changed strongly during SAR integrating time. The smearing due to this effect can be reduced and the obtained results can be improved by meeting the following conditions:
 - (a) Incidence angle should tend to be a minimal possible value (the slant range is reduced, thus a reduced Doppler shift).
 - (b) The wave height of swell should be in the range 0.5 m (must be well visible in SAR image) to ~5 m (higher wave amplitude means stronger non-linear effects by a moving surface)
 - (c) The acquisition (descending or ascending mode) should be selected in order to avoid azimuth traveling waves in SAR flight direction (rather opposite to azimuth traveling waves).
2. Radar reflection of water particles pulled out from the surface and flying in the air: this takes place by, e.g., wave breaking due to its critical steepness or due to hindrance like reef or by ship bow. The signatures in the image are the streaks pattern in location where the wave breaks, directed in azimuth (waves are going to SAR) or against azimuth (waves are going from the SAR sensor). The length of these streaks is connected directly to the speed of the flying particles (Doppler shift). Assuming that the maximum of this speed is equal to the orbital velocity at wave crest before breaking, wave amplitude can be estimated. The height of the breaking waves is also an indirect proof on underwater topography and can be used to detect dangerous locations (underwater reefs). This information can be successfully applied for ship safety and warning systems.

5.2 Optical methods

The application of the multispectral method to retrieve water depth depends on several sensor parameters and environmental recording conditions. For adequate recording conditions, clear atmospheric and in-water conditions, promising accuracies with a RMS of 8% to 20% between the optical product and echo sounding data could be achieved for a depth between 0.1 and 18 m at different coastal sites worldwide using IKONOS, QuickBird, and WorldView-2 satellite data. Reflecting the satellite sensor properties of QuickBird with only four bands and unknown radiometric calibration accuracy and taking into account the temporal shift of several years

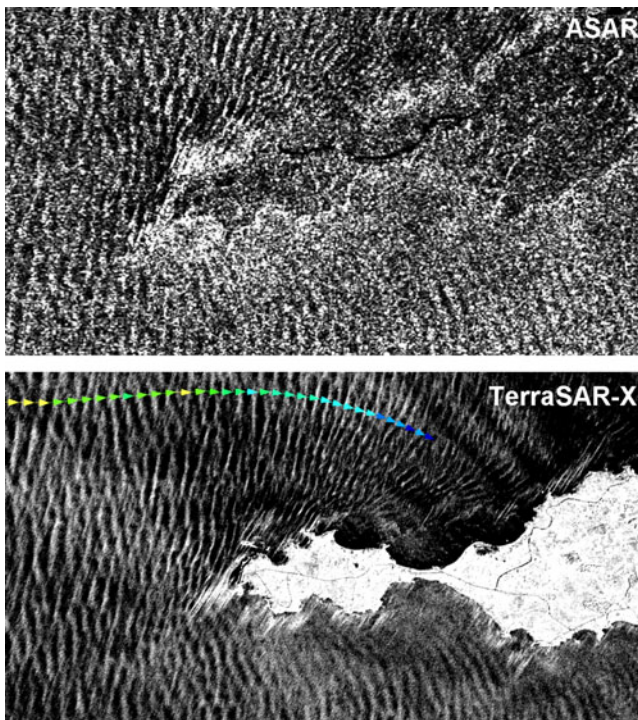


Fig. 15 Rottenest Island, ASAR (resolution ~25 m, image pixel size 12 m) and TerraSAR-X Spotlight (resolution ~2 m, image pixel size 0.75 m): Although the waves are detectable in ASAR images, the extraction of wavelength <200 m and obtaining a refraction of quality necessary for underwater topography estimation is not possible

and assumed spatial mismatch between the data sets of several meters, we interpret this as a good result. Comparable results with a similar processing procedure were retrieved for inland waters such as Lake Constance in Germany and coastal sites (Ningaloo Reef, Australia) using hyperspectral airborne data. The validation here confirms the good results for bathymetry (e.g., RMS of 0.15 m in Lake Constance at 0–4 m; RMS 8% for the Ningaloo Reef at 0–15 m).

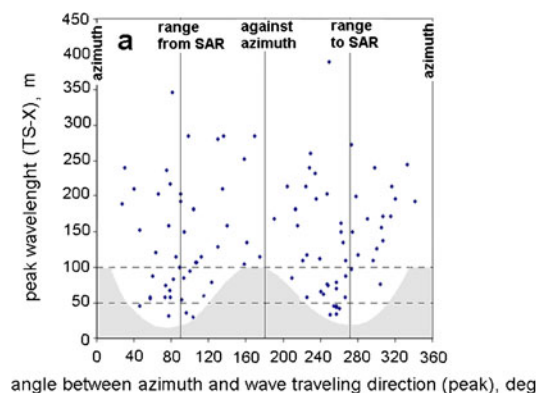


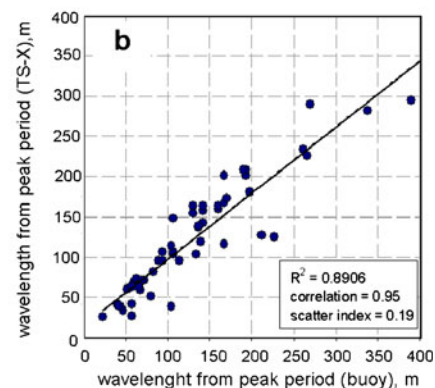
Fig. 16 Distribution of peak wavelength over a direction from 100 TS-X scenes acquired in North Sea—the cutoff is gray-colored (wavelength of about 30 m for range and about 100 m for azimuth

However, the operational application of this approach requires accounting for all the possible and critical recording conditions. Atmospheric turbidity, sun glitter effects, and adjacency scattering from bright land targets: these parameters all contribute to the reflected signal—in the whole range of channels from the visible to the infrared region. Many of the multiple, influencing parameters cannot be discriminated because of physical reasons using multispectral sensors with only one channel in the infrared region. The same applies for the in-water optical conditions, when changing water constituent concentrations exceed a certain range. Therefore, the method is so far restricted to clear atmospheric and in-water conditions; otherwise, a decreased sensitivity with increasing depth must be accepted. However, with an increasing number of spectral channels available with, e.g., Worldview-2, we could eliminate even varying aerosol concentrations with better accuracy. The coupled retrieval with varying in-water turbidity is still in investigation.

The forecast of the sun glitter impact to specific geometrical recording conditions is essential for the planning of surveys. Therefore, we started systematic investigations of the theoretical calculated sun glitter impact as well as the practical impacts to both high- and low-resolution satellites such as Rapideye, Worldview-2, and MODIS.

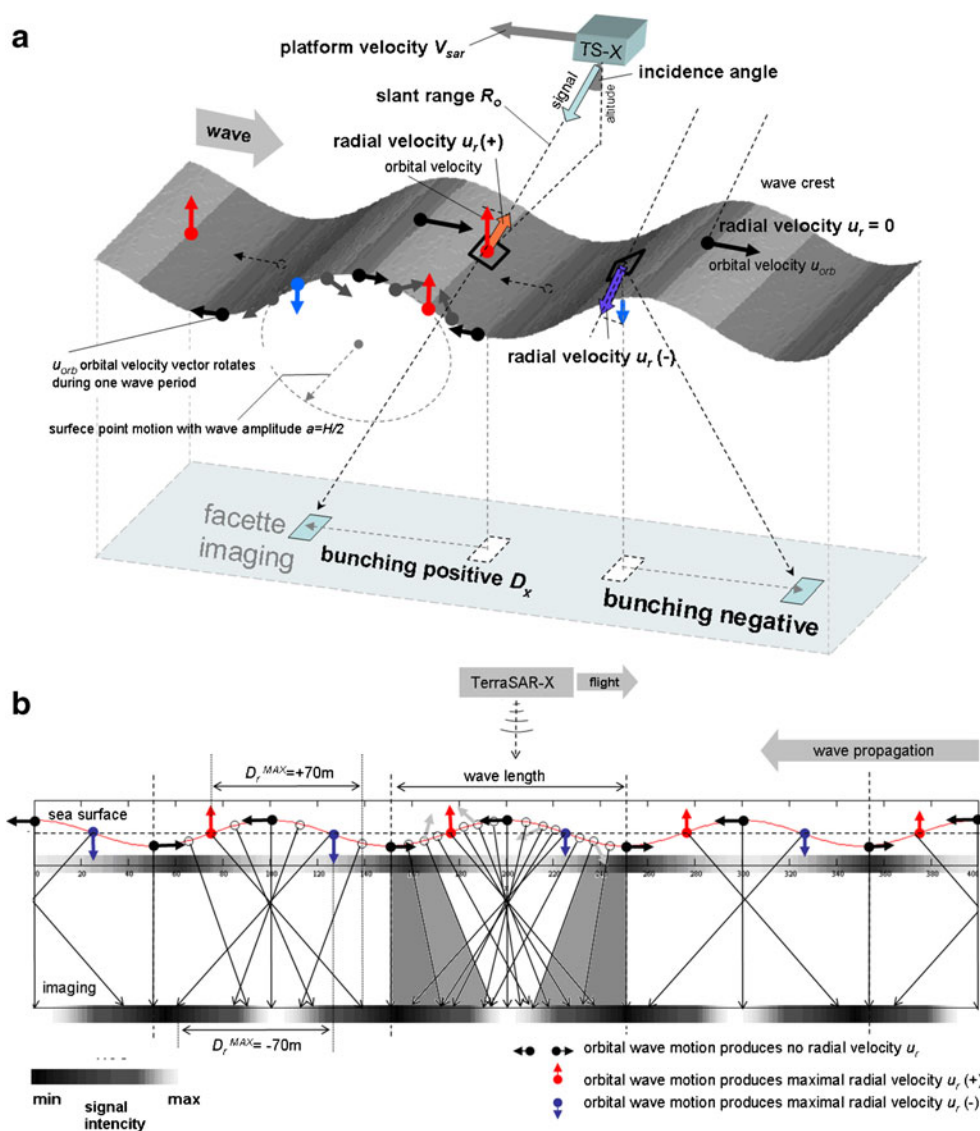
6 Summary

A practical approach for exploring of bathymetry by the synergetic use of multiple remote sensed data sources for coastal areas is presented. The SAR-based method uses refraction of swell waves and covers the depth domain between 100 and 10 m. The optical-based method uses sunlight reflection analysis and covers the depth interval shallower than 20 m.



directions) (a). Scatter plot for peak wavelength derived for collocated buoys (NDBC 44066 28 entries and by Ecosfisk Platform 27 entries) and TS-X (b)

Fig. 17 Imaging of waves ($L=100$ m, $a=1.5$ m, $T=10$ s, $u_{orb}=0.98$ m s^{-1}) traveling in azimuth and opposite to the satellite flight direction. Velocity bunching due to wave orbital velocity ($D_x=R_o \cdot u_r/V_{sar}=75$ m for $\theta=22^\circ$): Although the imaging mechanism is non-linear, the replacing of the facets remains inside of one wavelength by swell wave for TerraSAR-X characteristics (ground speed and slant range). The wave is imaged “turned” in the location of its own; the image is focused around a wave crest. The 3D image (a) shows a projection of orbital velocity to sensor; image b shows a 2D scheme of wave imaging



The underwater topography is obtained with accuracy in the order of 15% for depths 60–20 m using a SAR-based method. The estimation accuracy is generally dependent on sea state (swell availability) and its acquisition quality. The latter is influenced by artifacts, nonlinear SAR imaging effects, and the complexity of the topography itself (e.g., reefs cause wave breaking).

Additionally, the SAR-based methodology allows the detection of shoals (underwater mountains, reefs, deposited sand bars) with depths <30 m even if the quality of sea state is insufficient for obtaining the topography with the aforementioned accuracy. The remotely sensed information on shoals detected can be integrated into maritime ship safety concepts. Furthermore, this kind of data is considered as valuable in areas like German Bight, where topography changes comparably fast due to soft seabed by storms so that official charts can be out of date. The synoptic and frequent in situ

measurements of the German Bight are complicated and expensive procedures. Therefore, the obtained information can be tactically used for supporting in situ measurements performed with, e.g., ship-borne sonar by pointing out the shallow locations to be updated.

With regard to the optical methods, the MIP data processing is stable, applicable for extensive mappings, and worldwide transferable. For the shallow water region presented here from 0 to 18 m, we obtained a deviation of about 20%. The limitations of methods as described in the discussion must be accounted for in operational applications. However, new opportunities come up also with the challenges: Optical satellite records with a high impact of sun glitter are of limited use for the multispectral methods as discussed. However, such scenes can be used in a similar way to derive bathymetry using the dispersion relation as described in the SAR part of this paper, with the same environmental precondition to the wave field.

The sun glitter impact and sea surface roughness parameters can be quantified and retrieved from multispectral images using pixelwise sun glitter impact algorithms. Clearly visible is the effect in the infrared bands where only atmosphere and the sea surface reflection contribute to the sensor signal.

First tests of this synergetic approach of SAR and optical remote sensing data open a new possibility to find out the underwater structures and estimate the depth maps in the coastal areas worldwide. The combination of the obtained bathymetry with that for above-water topography from TanDEM-X satellite mission can be applied to retrieve the complete digital elevation model.

Acknowledgments This study is supported by projects DEEPVIEW (Bathymetry from TerraSAR-X und RapidEye Satellites, supported by the Space Agency of the German Aerospace Center DLR, FKZ 50EE0821 and 50EE0837) and PAROL Ship Security (TSX data are provided by DLR science AO). Echo sounding data are provided by Western Australian Department for Planning and Infrastructure. Special thanks to M. Kobryn and M. Harvey for processing and provision of the Rottenest data.

Appendix

NRCS, RAR modulations, and azimuthal cutoff

The normalized cross-section NRCS is a dimensionless variable denoted by σ_0 , which is usually given in dB values. The normalization of NRCS is done by dividing the radar echo by the incident power. The basic object imaged by a SAR is the complex reflectivity r , with a magnitude related to the NRCS as follows:

$$\sigma_0 = \langle |r|^2 \rangle \quad (10)$$

and a phase which accounts for possible phase shifts taking place in the scattering process. Since the phase of reflectivity r is very sensitive to the detailed geometry of the local scattering process, r it is usually taken as a random circular Gaussian process with second moments related to the NRCS by Eq. A1. The angle brackets mean an averaging over a resolution cell. The NRCS in dB values is (Holt, 2004):

$$\sigma_0^{\text{dB}} = 10 \cdot \log(\sigma_0/A) \quad (11)$$

where A is the calibrations constant “energy reflected in an isotropic way”—scatter back to the antenna over a specified area (Holt, 2004).

For the ocean surface, the NRCS is related to the spectral wave energy F contained in the short ripple waves (surface capillary waves with $f > 10^{-1}$ Hz) with Bragg wave number k_B by

$$\sigma_0 = \gamma_G [F(k_B) + F(-k_B)] \quad (12)$$

where γ_G is a factor depending on incidence angle, polarization, and the dielectric constant of sea water (Valenzuela 1978).

All three RAR modulation mechanisms assumed to be independent, the expression for the sum effect for the respective transfer functions is:

$$T_k^R = T_k^{\text{tilt}} + T_k^{\text{hydr}} + T_k^{\text{rb}} \quad (13)$$

where T_k^{tilt} is the tilt modulation (local sea surface slope changing by wave), T_k^{hydr} is hydrodynamic modulation (surface roughness influenced by orbital wave motion), and T_k^{rb} is range bunching (geometric effect by slanting line-of-sight).

For the moving antenna, an ocean wave imaging mechanism, which in general has to be taken into account for scanning systems like SAR, is the so-called scanning distortion. This effect causes a shearing of the imaged ocean waves due to the radar platform velocity. As the ocean wave phase speed c_p , the mechanism can be readily modeled by applying the following transformation in the spectral domain (Schmidt, 1995):

$$k'_x = k_x - \frac{c_p}{V_{\text{SAR}}} |k|, \quad k'_y = k_y \quad (14)$$

where (k_x, k_y) are the original wave numbers referring to the underlying ocean wave field and k'_x and k'_y are the corresponding wave numbers in the respective scanned image. As the ratio of phase speed to platform velocity c_p/V_{SAR} for space-borne SAR systems like the TS-X SAR is negligibly small (< 0.01), it can be neglected in the study. However, the effect can be significant for airborne systems (Schulz-Stellenfleth and Lehner, 2002).

The sea surface motion by waves leads to a velocity component u_r of a backscattering ocean surface facet towards the radar (slant range). SAR determines the azimuth position of backscattering objects by recording the Doppler history of the returned signals. The resulting effect is a shift of the corresponding SAR imaged point in flight direction by a distance (Valenzuela, 1978):

$$D_x = \frac{R_0}{V_{\text{SAR}}} u_r \quad (15)$$

The sign convention for u_r is such that positive velocities indicate a movement of the imaged facet towards the radar. For SAR imagery acquired over land, this effect is known as the “train off the track” effect. In the case of the ocean waves, the periodic movement of the surface leads to an alternate stretching and bunching of image intensities in azimuth (velocity bunching). This effect is particularly strong for in-azimuth-direction traveling waves. It culminates in the fact that azimuth traveling waves, which are shorter than a certain thresh-

old, are not visible by imaging in SAR. This threshold is called SAR azimuth cutoff wavelength. When the wave height is too large, wave orbital velocities also grow large, and the scatterers can be shifted by more than one long ocean wavelength in azimuth. This effectively degrades the azimuth resolution. An empirical solution for the minimum detectable azimuth wavelength by a SAR cutoff wavelength L_{\min} is given by:

$$L_{\min} = C_0 \frac{R_0}{V_{\text{SAR}}} H_s^{1/2} \quad (16)$$

where H_s is ocean significant wave height and C_0 is a constant of order 1 with units ($\text{m}^{1/2} \text{s}^{-1}$) (Holt, 2004). This latter limitation is a crucial factor in SAR wave images. For polar-orbiting free-flying SAR satellites, R_0/V_{SAR} is about 120 s. Thus, for $H_s = 4$ m, the minimum detectable azimuth wavelength is 240 m, with the resolution further degrading in higher sea states (Holt, 2004). For ENVISAT, this parameter is about 114 s by an altitude of 800 km, $V_{\text{SAR}} = 7.55 \text{ km s}^{-1}$, and $\theta = 22^\circ$. For TS-X $R_0/V_{\text{SAR}} \sim 77$ s for incidence angle $\theta = 22^\circ$ and L_{\min} according to Eq. 16 and $L_{\min} = 155$ m for $H_s = 4$ m and 109 m for $H_s = 2$ m. Due to its lower orbit compared to ERS1/2 and ENVISAT, TerraSAR-X has a quite short azimuth cutoff wavelength of around 100 m according to the theory for a sea state of 2.0 m significant wave height. Therefore, TerraSAR-X is able to detect the shoaling of short waves. The shortest near-shore azimuth traveling waves observed in TS-X scenes have a wavelength of 70 m (Lehner et al., manuscript submitted for publication).

The statistics for the distribution of peak wavelength over a direction from 100 TS-X scenes acquired in North Sea are shown in Fig. 16a (Bruck and Lehner, 2010). A number of images were acquired over buoy locations in order to investigate the TS-X capability of wave imaging. Figure 16b shows a scatter plot for peak wavelength derived from collocated buoy measured peak period by deep water relation and TS-X-derived peak wavelength for NDBC buoy 44066 ($39^\circ 34' 59''$ N $72^\circ 36' 2''$ W) and the buoy located near Ekofisk oil platform in North Sea ($56^\circ 10' 03''$ N $3^\circ 32' 32''$ E). The statistical comparisons (scatter index is 0.19, correlation is 0.95, mean square error 0.89) show a good agreement with in situ data.

Figure 17 shows that the scheme of radial velocity originates from orbital motion and velocity bunching for the imaging of azimuth traveling waves (Fig. 17a, b). The scheme displays that, for the swell waves of 100 m in wavelength and traveling in azimuth direction, the wave imaging mechanism is non-linear. However, the SAR-imaged waves keep the original wavelength value. Although the wave is imaged “turned” in its own location, the image is focused around its crest.

References

- Abreu LW, Anderson GP (1996) The MODTRAN 2/3 report and LOWTRAN 7 model. Ontar Corporation, 260 pp
- Alaee MJ, Charitha Pattiaratchi C, Ivey G (2007) Numerical simulation of the summer wake of Rottnest Island, Western Australia. *Dynamics of Atmospheres and Oceans* 43:171–198
- Albert A, Mobley CD (2003) An analytical model for subsurface irradiance and remote sensing reflectance in deep and shallow case-2 waters. *Opt Express* 11:2873–2890
- Alpers W, Hennings I (1983) A theory of the imaging mechanism of underwater bottom topography by real and synthetic aperture radar. *Journal of Geophysical Research* 99:10529–10546
- Alpers WR, Rufenach CL (1979) The effect of orbital motions on synthetic aperture radar imagery of ocean waves. *IEEE Trans Antennas Propag* 27:685–690
- Breit H, Fritz T, Bals U, Lachaise M, Niedermeier A, Vonavka M (2010) TerraSAR-X SAR processing and products. *IEEE Transactions on Geoscience and Remote Sensing*, vol. 48, no. 2. February, 0196–2892
- Brusch S, Held P, Lehner S, Rosenthal W, Andrey Pleskachevsky (2011) Underwater bottom-topography in coastal areas from TerraSAR-X data. *International Journal of Remote Sensing* (in press)
- Bruck M, Lehner S (2010) Extraction of wave field from TerraSAR-X data. *Oceanography workshop SEA-SAR 2010. Advances in SAR oceanography from ENVISAT, ERS and ESA third party missions, ESA ESRIN, Frascati/Rome, Italy, 25–29 January 2010*
- Fan K, Huang W, He M, Fu B (2008) Simulation study on optimal conditions for shallow water bathymetry observation by SAR. In *IGARRS, 7–11 July, MA, USA*
- Flampouris S (2010) On the wave field propagating over an uneven sea bottom observed by ground based radar. *Dissertation, GKSS, Institute of Coastal Research 2010/6, ISSN 0344-9629*
- Green E, Edwards A, Mumby P (2000) Mapping bathymetry. In: Edwards A (ed) *Remote sensing handbook for tropical coastal management*. UNESCO, Paris, pp 219–235
- Hasselmann K, Raney RK, Plant WJ, Alpers W, Shuchman RA, Lyzenga DR, Rufenach CL, Tucker MJ (1985) Theory of synthetic aperture radar ocean wave imaging: a MARSEN view. *J Geophys Res* 90:4659–4686
- Heege T, Bogner A, Häse C, Albert A, Pinnel N, Zimmermann S (2003) Mapping aquatic systems with a physically based process chain. *Proc. 3rd EARSeL Workshop on Imaging Spectroscopy, Herrsching, 13–16 May 2003*. Edited by M. Habermeyer, A. Müller, S. Holzwarth. ISBN 2-908885-26-3, pp 415–422
- Heege T, Fischer J (2004) Mapping of water constituents in Lake Constance using multispectral airborne scanner data and a physically based processing scheme. *Can J Remote Sensing* 30(1):77–86
- Heege T, Hausknecht P, Kobryn H (2007) Hyperspectral seafloor mapping and direct bathymetry calculation using HyMap data from the Ningaloo reef and Rottnest Island areas in Western Australia. *Proceedings 5th EARSeL Workshop on Imaging Spectroscopy, Bruges, Belgium, April 23–25 2007*, p 1–8
- Heege T, Kobryn H, Harvey M (2008) How can I map littoral sea bottom properties and bathymetry? In: Fitoka E, Keramitsoglou I (eds) *Inventory, assessment and monitoring of Mediterranean wetlands: mapping wetlands using earth observation techniques*. EKBY & NOAA. MedWet (scientific editor Riddiford NJ)
- Heege T, Kiselev V, Odermatt D, Heblinski J, Schmieder K, Tri Vo K, Trinh Thi L (2009) Retrieval of water constituents from multiple earth observation sensors in lakes, rivers and coastal zones. In:

- Proc. IEEE International Geoscience and Remote Sensing Symposium IGARSS, Cape Town, South Africa
- Hemer MA, Simmonds I, Keay K (2007) A classification of wave generation characteristics during large wave events on the Southern Australian margin. *Continental Shelf Research* 28(4–5):634–652
- Henning I (1990) Radar imaging of submarine sand waves in tidal channels. *Journal of Geophysical Research* 95:9713–9721
- Holden H, LeDrew E (2002) Measuring and modeling water column effects on hyperspectral reflectance in a coral reef environment. *Remote Sensing Environ* 81(2–3):300–308
- Hessner K, Reichert K, Rosenthal W (1999) Mapping of sea bottom topography in shallow water by using a nautical radar. In 2nd International Symposium on Operationalization of Remote Sensing, 16–20 August 1999, Enschede, The Netherlands
- Holt B (2004) SAR imaging of the ocean surface. In: Jackson CR, Apel JR (eds) *Synthetic Aperture Radar (SAR) marine user's manual*. NOAA NESDIS Office of Research and Applications, Washington, DC, pp 25–79
- Kisselev V, Bulgarelli B (2004) Reflection of light from a rough water surface in numerical methods for solving the radiative transfer equation. *J Quant Spectrosc Ra* 85:419–435
- Komen GI, Cavaleri L, Donelan M, Hasselmann K, Hasselmann S, Janssen PAEM (1994) *Dynamics and modeling of ocean waves*. Cambridge University Press, UK, 554 p
- Lafon V, Froidefond JM, Lahet F, Castaing P (2002) SPOT shallow water bathymetry of a moderately turbid tidal inlet based on field measurements. *Remote Sensing of Environment* 81:136–148
- Lehner S, Schulz-Stellenfleth J, Brusch S, Li XM (2008) Use of TerraSAR-X data for oceanography, EUSAR 2008, 7th European Conference on Synthetic Aperture Radar. Friedrichshafen, Germany
- Lehner S, Horstmann J, Koch W, Rosenthal W (1998) Mesoscale wind measurements using recalibrated ERS SAR images. *Journal of Geophysical Research* 103:7847–7856
- Li X, Li CH, Pichel WG (2006) SAR imaging of shallow water sand ridges aligned with tidal current. In *Ocean SAR*, 23–25 October 2006, St. John's, NL, Canada
- Lionello P, Günther H (1992) Assimilation of altimeter data in a global third-generation wave model. *Journal of Geophysical Research* 97(C9):14,453–14,474
- Lyzenga DR, Shuchman RA, Lyden JD (1985) SAR imaging of waves in water and ice: evidence for velocity bunching. *J Geophys Res* 90:1031–1036
- Mobley C (1994) *Light and water: radiative transfer in natural waters*. Academic, San Diego
- Pearce AF, Lynch MJ, Hanson CE (2006) The Hillarys Transect (1): seasonal and cross-shelf variability of physical and chemical water properties off Perth, Western Australia. *Continental Shelf Research* 26(15):1689–1729
- Pinnel N (2007) A method for mapping submerged macrophytes in lakes using hyperspectral remote sensing. Dissertation, Technische Universität München
- Piotrowski CC, Dugan JP (2002) Accuracy of bathymetry and current retrievals from airborne optical time-series imaging of shoaling waves. *IEEE Transaction on Geoscience and Remote Sensing* 40:2606–2618
- Philpot W (1987) Radiative transfer in stratified waters: a single scattering approximation for irradiance. *Appl Opt* 26(19):4123–4132
- Pleskachevsky A, Li X-M, Brusch S, Lehner S (2010) Investigation of wave propagation rays in near shore zones. Proceeding: Oceanography Workshop SEA-SAR 2010, Advances in SAR Oceanography from ENVISAT, ERS and ESA third party missions, ESA ESRIN, Frascati/Rome, Italy, 25–29 January 2010
- Playford PE, Leech REJ (1976) *Geology and hydrology of Rottneest Island*. Geological survey of Western Australia Report 6
- Romeiser R, Alpers W (1997) An improved composite surface model for the radar backscattering cross section of the ocean surface. 2. Model response to surface roughness variations and the radar imaging of underwater bottom topography. *Journal of Geophysical Research* 102:25 251–25 267
- Schneggenburger C, Günther H, Rosenthal W (2000) Spectral wave modeling with non-linear dissipation: validation and applications in a coastal tidal environment. *Coast Eng* 41:201–235
- Schmidt R (1995) Bestimmung der Ozeanwellen-Radar-Modulations-Übertragungsfunktion aus der Abbildung des Ozeanwellenfeldes durch flugzeuggetragene Radarsysteme mit synthetischer Apertur. Ph.D. thesis, Universität Hamburg
- Schulz-Stellenfleth J, Horstmann J, Lehner S, Rosenthal W (2001) Sea surface imaging with an across track interferometric synthetic aperture radar (InSAR)—the SINEWAVE experiment. *IEEE Trans Geosci and Rem Sens* 39(9):2017–2028
- Schulz-Stellenfleth J, Lehner S (2002) Spaceborne synthetic aperture radar observations of ocean waves traveling into sea ice. *J Geophys Res* 107, No. C8, 3106, [10.1029/2001JC000837](https://doi.org/10.1029/2001JC000837)
- Winkel N (1994) Modeling of waves in extreme shallow water. In GKSS-Research Center, ISSN 0344-9629
- Valenzuela GR (1978) Theories for the interaction of electromagnetic and oceanic waves—a review. *Boundary Layer Metereol* 13:61–85
- Vanderstraete T, Goossens R, Ghabour TK (2003) Bathymetric mapping of coral reefs in the Red Sea (Hurghada, Egypt) using Landsat7 ETM+ Data. *Belgeo*, No. 2003(3), pp 257–268